MASTER IN AERONAUTICAL ENGINEERING

2019-2020

FINAL MASTER THESIS

Dynamic analysis of a rotorcraft airborne wind energy system

Thesis by:

Carceller Candau, Javier

Thesis advisor:

Sánchez-Arriaga, Gonzalo

Supervisors at *IFP Energies Nouvelles*:

Tona, Paolino and **Pfister, Jean-Lou**

03/07/2020

Acknowledgements

First of all I would like to acknowledge my supervisors at *IFP Energies nouvelles*, Paolino Tona and Jean-Lou Pfister. Without the opportunity they have given me this work would not have been possible. The experience within the company will be stuck in me forever.

Also my supervisor at UC3M, Gonzalo Sánchez-Arriaga, whose help and know-how from all his works leading to the development of LAKSA have been precious.

Thank you very much Christof for the experimental data you have provided us. It is thanks to people like you, just looking for the best for the advancing of the technology, that the limits can be pushed beyond.

Finally, thank you very much to my family and specially to Selina, your support came always in the right moment, not only during the pursue of this thesis, but during the whole MSc.

Abstract

The goal of this thesis is to develop a dynamic simulator for rotorcraft airborne wind energy systems. These airborne wind energy systems have a strong potential to become part of the solution of the foreseeable energy problem and to be key in the decarbonization process of the energy production industry. They are aimed to exploit wind energy from the high winds, which are more intense and constant that near ground, where current wind turbines are placed. This helps overcome the difficulties that wind turbines show to be globally scalable.

Rotorcraft airborne wind energy systems are a particular case inside this new technology. It makes use of the autorotation concept that enhanced the development of the autogyro and that has been studied in the past to allow a safe descent of helicopters in the case of engine failure. Autorotation allows the rotor to extract energy from the wind, using part of this energy to stay on air and transmitting the excess of energy to the ground.

While autorotation and airborne wind energy systems have been the subject of numerous works and research, both in the hardware and in the software, their conjoint application is still to be mastered. In this thesis, the autorotation phenomenon has been thoroughly studied in order to build a dynamic model capable of reproducing with enough fidelity the behavior that a rotor would experience when submitted to wind. The model has been built into LAKSA, a Lagrangian Flight Simulator that allows for the dynamic simulation of several types of airborne wind energy systems, but that was lacking up to now a rotorcraft simulator. This thesis explores the fundamental variables of the problem to see how they affect the output. The simulator model has been built with the highest degree of generalization so that it is not restricted by a design. Overall, this work enhances the further development of the technology and shows that rotorcraft wind energy systems have the capabilities to become a reliable energy source.

Contents

List of Figures

List of Tables

Chapter 1

Introduction

Contents

We will run out of fossil fuels. That is for sure. But not only that. Burning fossil fuels accounts for most of the emission of gases responsible for the greenhouse effect. The current global and interconnected society needs energy to keep its pace and, far from heading towards a reduction in energy demand, it will force the energy industry to supply more energy, leaving a scenario of unsustainable growth of demand.

In such scenario, the major energy companies have made an effort in the last years to fund research and build all sort of renewable energy stations. That is the case of *IFP Energies nouvelles*, within which this thesis is carried out. *IFP Energies nouvelles* is a French public-sector research center, committed to work towards providing solutions that aim to solve the current challenges related to both energy and climate, envisioning a near future in which sustainable mobility and a more diversified energy mix are key.

Having in mind the effort put by this company and acknowledging the importance that any research in this field may have, when the opportunity to do this Master

Thesis at *IFP Energies nouvelles* appeared I was decided to go for it and take part in contributing to the future.

1.1 Motivation

The motivation behind the thesis can be divided into three main parts: my motivation, the motivation on *IFP Energies nouvelles* side, and the motivation behind the technology itself.

First of all, this thesis project has been a great opportunity to complete the educational background with an internship abroad, in a large research and development company committed to work for the future. For *IFP Energies nouvelles* it is the beginning of the research in a promising technology, by which they want to assess if it is a viable option for world-scaled energy harvesting. In September 2009 the G8 agreed to lower emissions of CO_2 by an 80% before 2050 [11], so lots of efforts are being made by the energy industry to achieve this goal. And, since the energy generation industry is more likely to have a rapid decarbonization than any other industry [12], they can set the path for other industries to follow.

Finally, the motivation behind studying Airborne Wind Energy Systems as a solution for the foreseeable energy crisis is based on its potential benefits over the current wind energy obtention systems: wind turbines. As stated in [2] “Nearly half of Europe’s existing wind farms will reach the end of their normal operational life by 2030”, meaning that they will have to be replaced. Replacing such amount of wind turbines will be an enormous expense, so finding a better and cheaper technology by 2030 is fundamental.

But prior to getting into more detail on the technology it is necessary to put it into context. During the year 2015 the energy production industry was held accountable for the emission of 2 billion metric tons of carbon dioxide, 99% of which was due to fossil fuels [13]. Here it lies the importance of substituting fossil fuels with alternative energy sources as soon as possible, rather than waiting until running out of them.

To be able to substitute fossil fuels in energy generation it is necessary for these alternative energy sources to be scalable to a global scale. The main alternative sources to face this challenge are nuclear, solar, hydropower and wind power. Let us analyze them.

1.1.1 Nuclear energy

Nuclear plants extract energy nowadays by the fission of Uranium-235 atoms in very energetic reactions that produce no carbon dioxide, hence not contributing to the greenhouse effect. This kind of energy generation system could be scalable and could be able to cope with world power demand, but it is not actually possible to rely on it in the long term. First of all because nuclear plants involve a worldwide hazard in case of accident, as it has already happened twice, in Chernobyl and Fukushima.

Furthermore it is found by [14] to be an expensive energy source, estimating in their study to cost in 2018 around 151$\$/MWh$, expensive compared to 60$\$/MWh$ for hydropower plants [15], 43$\$/MWh$ for onshore wind systems or 41$\$/MWh$ for solar energy, and this cost may underestimate the costs of storing nuclear wastes for thousands of years. Finally, the Intergovernmental Panel on Climate Change found it a serious risk and barrier for increasing the development of nuclear energy the concern that it may ease the ability of nations to develop nuclear weapons [12]. Therefore, it seems that nuclear energy can't be the solution.

1.1.2 Hydropower

Hydropower is the energy extracted from either fast-running water or water falling from a height distance. It has currently the highest portion of the electricity mix worldwide among the renewable energy sources as shown in Figure 1.1 for 2017 data.

However, it is not expected to experience a high increase in the forthcoming years since the large dams that make it possible to extract great amounts of energy from rivers are not harmless for its surrounding ecosystem. They alter the natural flow of the river, redirecting it, making areas that typically had water abundance to lack of it. They trap the natural cycle of sediments and also of seeds and water plants. The design of the dams must therefore be very careful with the location and the impact caused to the areas that live from the river. This makes it difficult to explode hydropower up to its maximum capabilities if the objective is to be able to obtain energy the least harmful way possible.

1.1.3 Solar energy

The Sun is evidently the most powerful energy source in the Earth and hence, solar energy seems to be a great candidate for solving the energy problem. However, it is one of the most intermittent energy sources, since it can only extract energy during daytime and it is also very susceptible to weather, since in cloudy days the solar radiation that gets to the solar panels is highly decreased.

But apart from the variability that solar energy shows, the world's energy demand is also variable, mainly seasonal. For example, in very warm countries the peak in power demand is found in the warmest days of summer, due to the air conditioning machines running all day long, while for more cooler countries, as in Europe, the peaks are found in the coldest days of winter, with more energy used for heating. This means that the energy that can be extracted must be known beforehand and must be adaptable to our needs. It is not the case of solar energy, whose output depends on external factors that cannot be controlled.

This means that it is not possible to rely on solar energy as the main energy source worldwide. The key is to be able to match offer with demand at any time. It

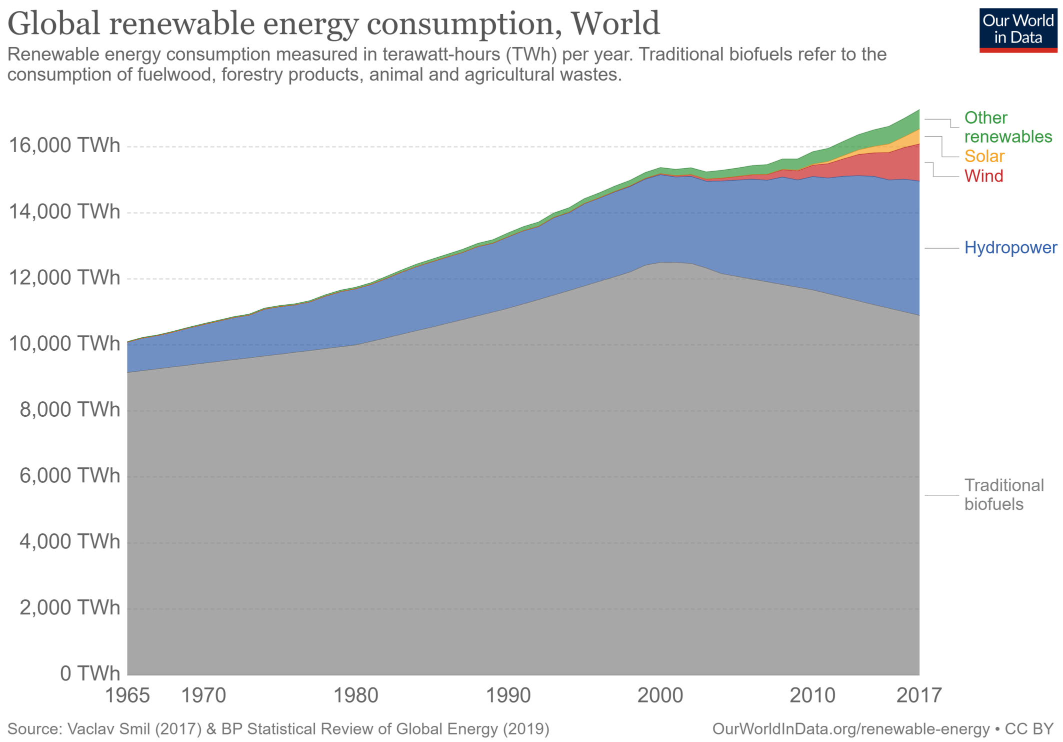

Figure 1.1: Graph of the global electricity mix evolution. Obtained from [1]

is true that it is always sunny somewhere, but it is not possible for half of the globe to provide energy for the whole world and, even in this case, the energy output would vary along the day. Figure 1.2 shows the great variability of solar energy generation, which allows for a capacity factor of less than 20% (it has evolved only from 15% to 18% in the last 9 years as shown in [16]). Solar photovoltaic cells show still a very low efficiency, so very little of the energy that the Sun's energy potential is effectively transferred into electricity.

This variability not only affects the capacity of solar energy. If solar energy could provide the average of electricity demand in the world, then the excess of energy generated when solar radiation is at its maximums should be stored for when no solar radiation hits the panels, or the excess generated when the world's demand is at its minimum to be used at peaks of demand. And this is actually a big problem. It would make solar energy much more expensive, due to the high costs of today's energy storage devices, but it would be even less efficient because of the high losses arising from energy storage and distribution.

1.1.4 Wind energy

Wind is an atmospheric phenomenon and, as such, is driven as well by the Sun. But in this case, extracting energy from wind is not extracting energy directly from the Sun. The heating of the atmosphere by the Sun causes very big masses of air to move, so part of the kinetic energy of these masses of air in movement can be

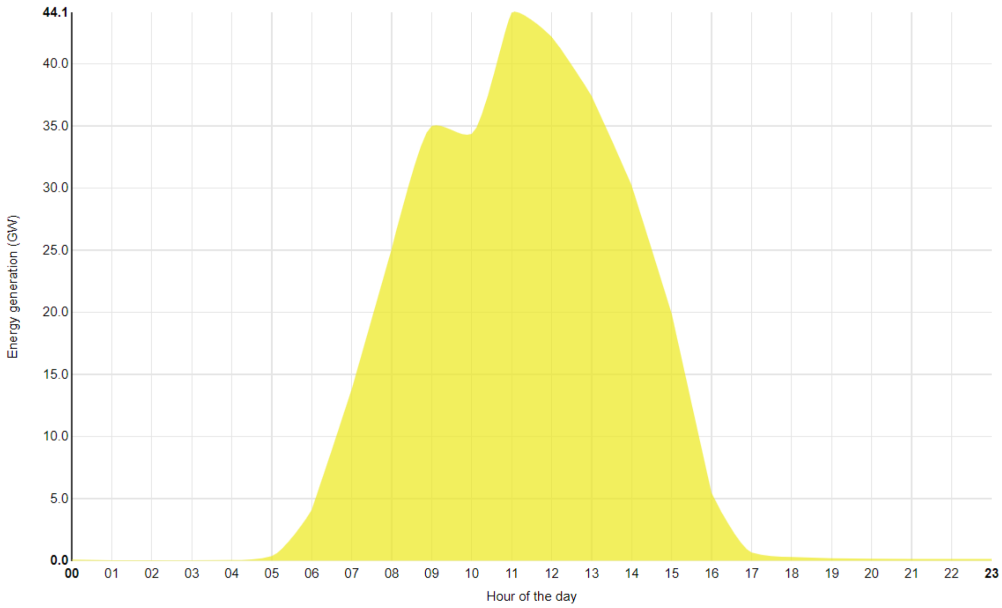

Figure 1.2: Solar energy generation in Europe for 11 March 2020. Source [2]

harvested. The power of the wind hitting a given object can be obtained as:

$$P = \frac{1}{2}\rho A V^3 \ . \tag{1.1}$$

This is, the power goes with the cube of the velocity, hence the great importance of looking for the locations with the fastest winds.

Wind energy currently generates electricity through fixed wind turbines. It is one of the renewable sources that have experienced the highest increase in the last few years. In 2019 wind energy accounted for the 15% of the EU electricity demand, and in this year a total of 13.2 GW of new wind power capacity were installed in EU providing a total of 205 GW, Spain being the country that installed the most of new onshore wind capacity (2.3 GW) [2].

However, 15% seems not enough to be the base of a carbon-free energy generation industry. In Denmark wind power was the primary energy source in 2019, accounting for as much as 48% of the energy mix [2]. The fact that in Denmark wind power accounts for a much larger part of its energy mix than the average of EU shows that certain locations are much more suitable for wind energy than others and, as well, that although it may be possible to rely on current wind energy technology in a small scale, it is much more complicated in a global scale.

As it happens with solar energy, it is not possible to rely solely on an energy source that may be insufficient in given circumstances. Wind energy shows as well a high variability, both in a day and along the year as shown in Figure 1.3.

Furthermore, the growth shown in the last years could slow down due to saturation of land areas where winds are suitable. It is not possible to cover all land

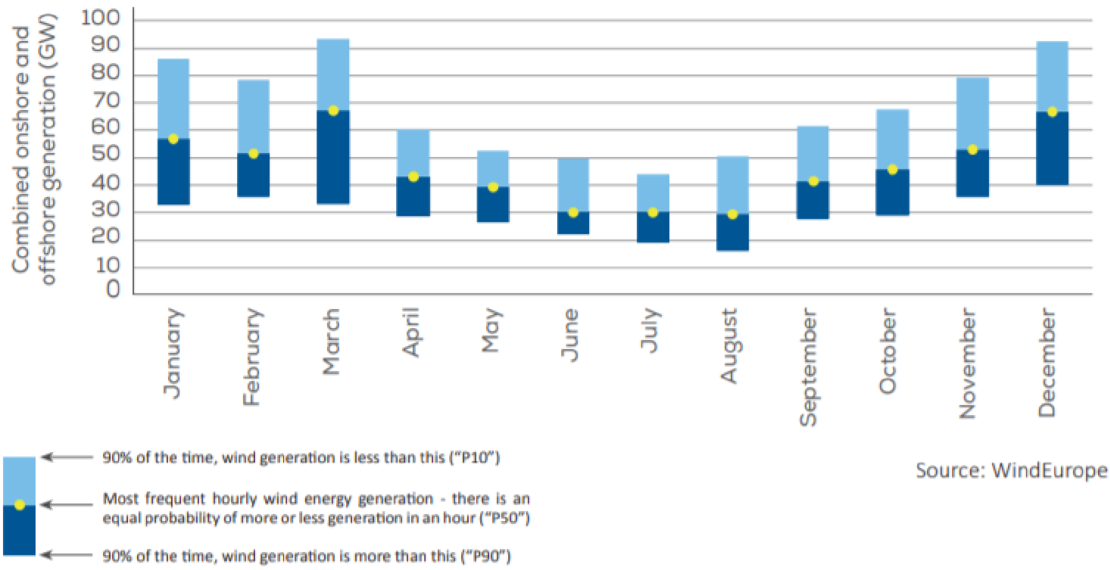

Figure 1.3: Spread of the hourly electricity demand covered by wind. Source [2]

available with wind farms, as it would be counterproductive to use wind turbines to obtain green energy at the cost of loosing green land. So one way to overcome this problem would be to leave land and build wind farms offshore. This has actually been the trend for countries such as UK, Germany, Belgium and Denmark that have been investing more in offshore wind than in onshore wind, as reflected in Figure 1.4. However they still are just 10% of total wind energy capacity. Two main reasons are behind this fact. First, that offshore plants cannot be placed anywhere, since they cannot be built if water depths are too high, so they should be near enough to the shore but far enough to not disturb shore activities and ecosystems. The second reason is that offshore LCOE (Levelized Cost of Energy) is 50% higher than that for onshore [16], due to the added difficulties of building offshore. But there is as well a big advantage for offshore wind farms that explains why some countries are heavily investing in it: winds offshore are stronger and more constant. This happens mainly in deep waters, so being able to explode wind energy very far from land would be a great benefit.

But the problem in wind variability can be avoided. Wind variability happens mainly at low altitudes, in the atmosphere's boundary layer, this is, the layer of air flow affected by the friction with a solid body. Going beyond this boundary layer, wind is generated thanks to differences in pressure and Coriolis forces, which provide winds that blow much more constantly and at higher velocities with low turbulence.

Studies by [17], [18] and [19] have shown that the power density of high altitude winds can be up to 17 kW/m^2, around two orders of magnitude higher than near ground. This result highlights the importance of the increase in velocity of the wind to generate more energy, since the result is much higher than for on-ground winds, even if with increasing altitudes the density diminishes. But recalling Equation 1.1, density is of order 1 while velocity is of order 3. If only a small amount of this wind

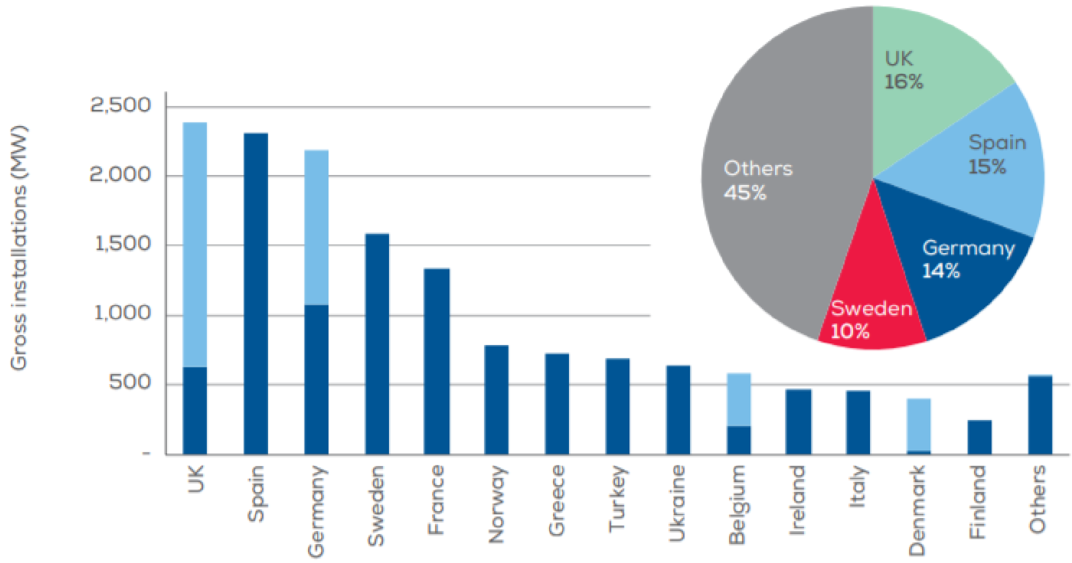

MW	UK	Spain	Germany	Sweden	France	Norway	Greece	Turkey	Ukraine	Belgium	Ireland	Italy	Denmark	Finland	Others
Offshore	1,764	-	1,111	-	-	-	-	-	-	370	-	-	374	-	8
Onshore	629	2,319	1,078	1,588	1,336	780	727	686	637	207	463	456	28	243	563
Total	**2,393**	**2,319**	**2,189**	**1,588**	**1,336**	**780**	**727**	**686**	**637**	**577**	**463**	**456**	**402**	**243**	**571**

Source: WindEurope

Figure 1.4: New onshore and offshore wind installations in Europe in 2019. Source [2]

power were available, harvesting energy at such high altitudes (this maximums of power density are for altitudes of 15000 ft and above) would not be interesting. However, wind power is considered to account for 100 times the power demand of the whole world [20].

To generate energy out of these high altitude winds it doesn't seem possible to rely on current wind turbines, which currently go up to heights of 70-80 m, even though higher towers are planned in the future. But very high altitudes for fixed wind turbines seem still not attainable, mainly due to weight restrictions. Therefore, new technology must be developed. This technology is Airborne Wind Energy Systems.

1.2 Airborne Wind Energy Systems. Current state of technology

Airborne Wind Energy Systems (AWES) is the technology that aims to be able to provide electricity worldwide from high altitude winds. This technology has been studied in the last years and several forms have been proposed, being the most extended one a system that has a tether attached to an aircraft with different working principles.

Research in this field started notably in the late 70s under the impulsion of the seminal work by [21] but the number of studies published was stagnant along the 90s. Since climate change and decarbonization began to really be taken seriously, research in this field regained interest and has exponentially increased, with some companies dedicated exclusively to this research, universities starting to play an important role, and with some energy companies and research centers now entering the field, as it is the case of *IFP Energies nouvelles*.

One of the most attractive aspects of AWES is that their potential may be able to scale up to the MW digits with a single plant [3], as demonstrated theoretically in [21] and [22]. This potential is not easily found in current renewable technologies up to date, and that makes AWES be one of the biggest current candidates to solve the future energy problem.

AWES can be divided mainly in two groups, depending on how they extract energy from the wind: ground-based systems and fly-gen systems. In both types of systems, the flying aircraft is attached to the ground by means of a tether, but the difference between both types resides in the fact that the tether could be transmitting mechanical energy (hence ground generation) or electricity (in case of onboard generation).

1.2.1 Ground-Based systems

Ground-based generation systems obtain energy in ground thanks to an aircraft in high altitude wind whose movement generates electricity in two possible ways. If the generator has a fixed base then electricity is generated by the unwind-rewind movement of the rope in the generator. If the generator has a moving base, then the aircraft itself moves the base along [3]. In any case, the aircraft in wind must be able to produce enough force to both keep itself on air and to move the rope or base.

For the fixed-base ground generation AWES electricity is produced in a cyclic way, each cycle containing two definite phases: a generation phase and a recovery phase. In the generation phase the aircraft is managed to follow a path, typically consisting in a "figure of eight ascending pattern" that produces high lift force that is used to unwind the rope (see Figure 1.5a). The use of the figure of eight pattern is due to the fact that it explodes crosswind flight that increases the relative wind that the aircraft experiences [3]. In the recovery phase part of the produced energy is used to drive a motor that rewinds the ropes to bring the aircraft to the initial position (see Figure 1.5b). The energy used for the recovery phase is much less than the one generated by using a control mechanism that maximizes the production of energy in the first phase and minimizes the energy consumption in the second [23].

The moving-base generation AWES arise from the search of a system that is always producing energy and not consuming it, since it further simplifies the electric grid to bring the energy to the electric network [3]. However they have still not been developed to the extent of the fixed-base systems although they are now beginning

(a) Generation phase (b) Recovery phase

Figure 1.5: Cycle of fixed-base ground generation systems. Obtained from [3]

to gain relevance. In this systems there is still unwinding and rewinding of the rope in the generator, but this acts only as a control mechanism and the energy is produced by the movement of the base thanks to the force generated by the aircraft. The moving phase systems can adopt several shapes, such as the vertical axis (see Figure 1.6a), closed loop rail (see Figure 1.6b), and open loop rail (see Figure 1.6c).

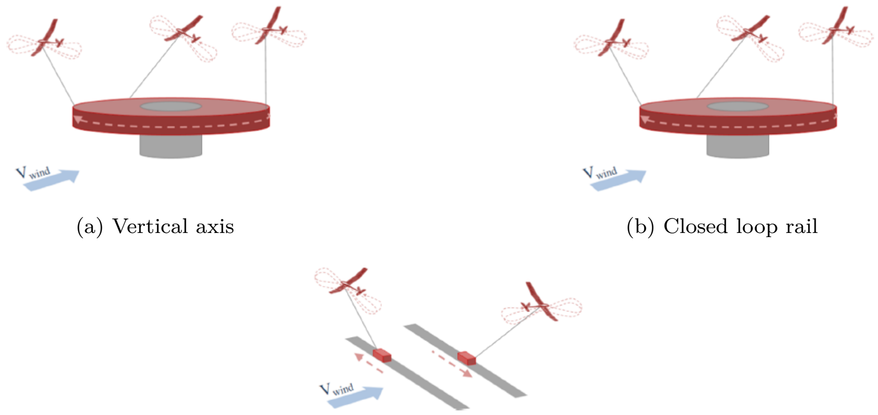

(a) Vertical axis (b) Closed loop rail

(c) Open loop rail

Figure 1.6: Moving base ground generation systems. Obtained from [3]

The aircrafts used in this kind of systems can take several forms, mainly being kites or gliders, as shown in Figure 1.7. Further information on the specifics of each type of aircraft can be found in [3].

There exists another design possibility that is not shown in Figure 1.7, mainly because it doesn't use a kite. It is the design that Christof Beaupoil uses in [4] and it is based on a rotor under autorotation. This rotor generates a lift force to keep it on air and an excess of rotation moment to make a ground station rotate, thanks to a structure called Open Tensegrity Shaft that transmits torsion from rotor to ground. Figure 1.8 shows this design. Since this will be actually the kind of AWES that will be used in this thesis, extended information will be given on its working characteristics along Chapters 2, 3 and 4.

The company that has been one of the pioneers in researching and developing ground generation systems is *KiteGen*. *KiteGen* is a company founded in Italy

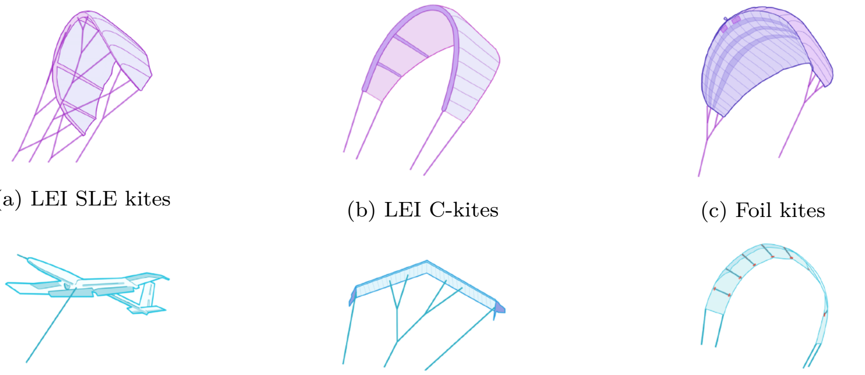

(a) LEI SLE kites (b) LEI C-kites (c) Foil kites

(d) Glider (e) Swept rigid wing (f) Semi-rigid wing

Figure 1.7: Types of aircrafts used in Ground-generation AWES. Obtained from [3]

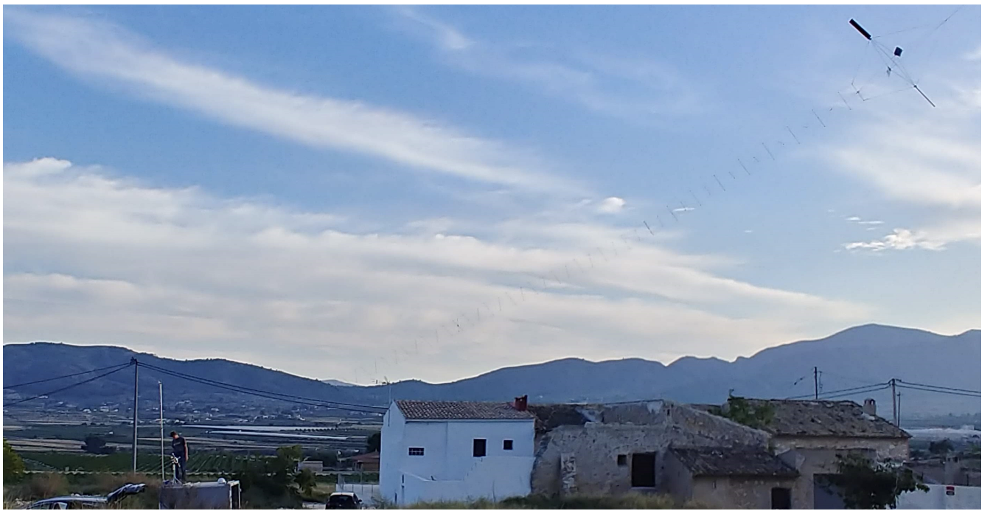

Figure 1.8: Ground-based AWES with a rotor in autorotation. Source [4]

with more than 10 years of research in the AWE field, having achieved already 5 prototypes that are near the industrialization phase (they are at TRL 8) [5]. They have obtained through their prototypes a design that is said to provide energy from wind with an LCOE of less than €30/MWh, which is more than €10/MWh less than current wind turbines.

One of their latest designs is the *KiteGen* Stem Generator, shown in Figure 1.9. It is an igloo structure attached to ground holding all the energy generation equipment that has two arms or stems that move to control and drive the kite. The kite, typically an arch-kite or semi-rigid wing (Figure 1.7f) is attached to the stems by using Dyneema ropes. They had a 3MW nominal power rating test site for this machine, but they tested it at 40kW since they had still not produced a kite rated for such energy generation.

But apart from *KiteGen*, there are several other projects currently under development:

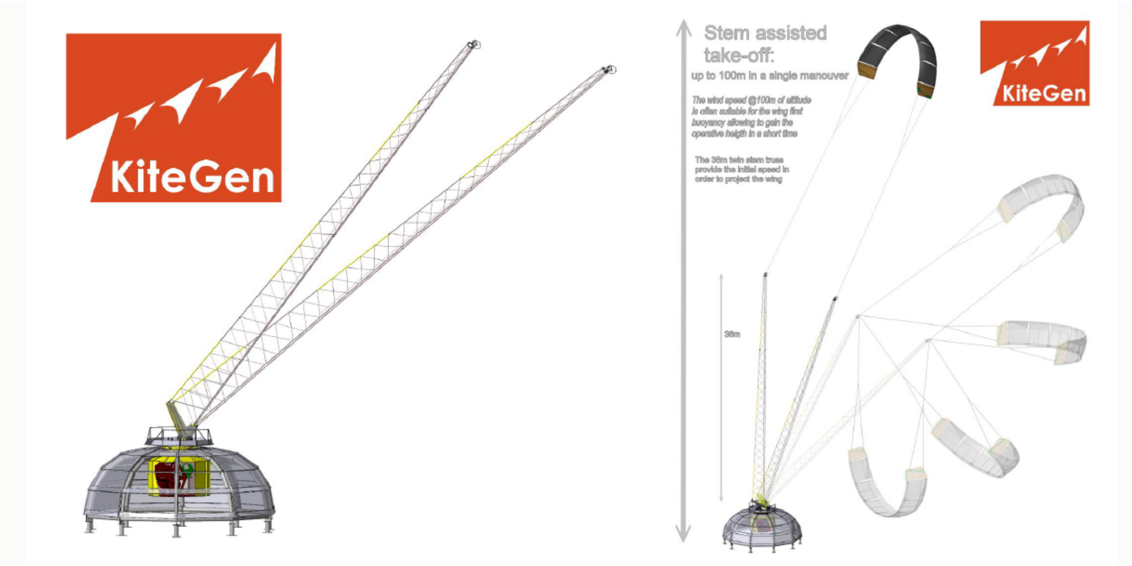

Figure 1.9: KiteGen Stem Generator, obtained from [5]

- *Kitenergy* is another italian company that has been able to test a $60kW$ prototype that controls a foil kite (Figure 1.7c) with two ropes, similar to *KiteGen* as it was founded by a former partner of this company [3].
- *SkySails* is a German company that develops ground generation AWES based on foil kites (Figure 1.7c) controlled with one rope. They are currently building prototypes to reach up to $3.5MW$ [3].
- *TU Delft* is the university whose project, KitePower, has obtained the biggest progress up to now. They are currently developing a $100kW$ prototype having in mind its launching for commercial applications [24]. It is a LEI kite with a single tether and they can control the angle of attack [3].
- *AMPYX Power* was the first company to develop a ground-generation AWES based on a glider (Figure 1.7d). Furthermore, their prototype is able to make the whole sequence from take-off, energy generation and landing automatically [3].

1.2.2 Fly-gen systems

In fly-generation AWES the energy is produced on-board by means of generators that act similar to a wind turbine but in a much smaller scale. Systems working with this principle can have very different shapes: kites or aircrafts flying crosswind, balloons rotating with Magnus effect or static rotors.

When using this types of systems, there is no need of reel in-out cycles to produce energy so other simple trajectories such as the circular one may be used for its simplicity and good output [3]. This simple figures facilitate the building of wind-farms in tighter spaces, making sure that trajectories will not intersect. Energy is provided to the machine only at the take-off phase, which makes the electric grid used for these systems much easier than that for fixed ground generation systems.

The company that has been the most successful up to now in the fly-gen systems is *Makani Power*. Founded in 2006, *Makani* started developing ground generation systems using fabric kites. They were acquired by *Alphabet* (Google matrix) in 2013, which boosted their capabilities. With *Alphabet* support, they began in 2015 the testing of a fly-gen AWES prototype that consisted of an aircraft flying crosswind and having a series of generators along the wing. This prototype was designed to transfer a total of 600 kW of electrical power (see the prototype in Figure 1.10). *Makani* obtained a successful demonstration in 2019 [6]. Unfortunately, at the beginning of 2020 *Alphabet* cut out *Makani's* project, and they are still looking for a solution to stay alive.

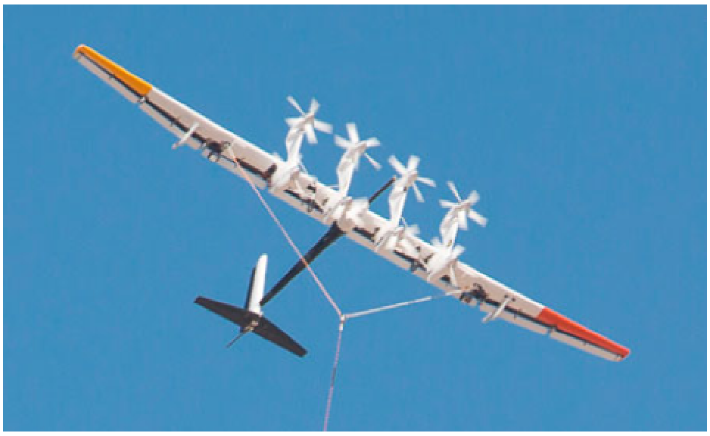

Figure 1.10: Makani Power 600 kW demonstrator. Source [6]

Some other companies are already developing fly-gen systems, such is the case of:

- *Joby Energy* uses a machine similar to that of *Makani* but consisting of a bi-plane structure [3].
- *Sky Windpower* was the first company to try a different concept. Instead of a glider type of aircraft, their prototype was a quadrotor whose rotors act as motors for take-off and then change to generators, entering into autorotation [3]. However, they had to close.

1.2.3 Other benefits and drawbacks

AWES offer some benefits with respect to current ways of extracting energy from the winds that go beyond the fact of using the more constant and intense winds found at high altitudes.

For example, high altitudes have the advantage of diminishing bird strike issues and they generate less noise in the nearest communities. But even more important, high altitude winds unlock the feasibility of extracting energy from wind practically in any location, it levels the wind availability worldwide.

Even if AWE would not be feasible for worldwide energy generation, it offers a key advantage not found elsewhere. It is an electricity generation system very rapidly deployed and with enough capacity to be useful in, for example, zones devastated by some natural disaster. They can be transported in a single truck, with weights of up to 30 tonnes and be installed by just laying them on ground in a flat surface with enough clear space for take-off.

Related to the simplicity and low weight of the components of AWES, they can be easily used offshore. And since they don't need as strong and complex foundations they don't have the constraint of being near the shore, so they could potentially be used to build windfarms in deep waters, were winds blow strongest and more steady. Only an anchor could be required for placing the "ground" structure.

Finally, on the other hand, the main drawback that is found for this technology, with the aim of scaling it to worldwide use, is that at high altitudes it may affect air traffic. Therefore, not any location could be used to build an AWE farm, and lots of regulation will be needed to make sure that this technology can be implemented with safety.

1.2.4 Current state of software

Up to this section the current state of the hardware of the technology has been discussed. But to deeply get an understanding of the extent of this work, also the current state of the software in AWES must be assessed. Several types of AWES have been developed and are approaching the commercialization phase. In this respect, a lot of software effort has been put in the proper simulation of AWES, as it is the case of the work done by this thesis' supervisor [25], [26], [27], [28], [29] and [30] that lead to the development of LAKSA, a Lagrangian Kite Simulator that includes several number of modules, each aimed at the simulation of a given type of AWES. However, it did not include up to now a module for Rotorcraft Airborne Wind Energy Systems (RAWES from now on), which this work will focus into. RAWES have not received as much attention up to now as the other types of AWES but they show a great potential as well.

Most of the research found in this field (RAWES) is aimed at the study of autorotation, the physical phenomenon behind RAWES, but the study of autorotation for energy extraction has not been highly exploited. Mackertich submitted his university MSc Thesis regarding RAWES [31], but its purpose was mainly to apply Glauert equations to study autorotation and then apply a simple method to estimate energy extraction. De Schutter, Leuthold and Diehl in their paper [32], study how controlling RAWES with pitch control onboard is possible. They model a RAWES similar to the one in this work but simplified to isolate the results of the particular study they are performing. For that reason, this is expected to be the first purely dynamical simulator for RAWES.

1.3 Objectives

The research objectives, specific for this thesis, that are being pursued here are:

- To learn how this new technology for extracting energy works.
- To analyze the current state of the art of rotorcraft airborne wind energy system.
- To acknowledge the relevance of this field of research.
- To develop a dynamic simulator of rotorcraft airborne wind energy system that will allow *IFP Energies nouvelles* to understand what are the strengths and weaknesses of such systems.
- Contribute to achieving decarbonization in energy production.

1.4 Thesis organization

This thesis aims to develop a dynamical simulator for rotorcraft airborne wind energy systems. Once this field has been introduced, Chapter 2 sets the basis of the physics behind the phenomenon of autorotation and establishes all the equations that build the model of the rotorcraft airborne wind energy machine for its simulation. Chapter 3 assesses the validation and verification of the model developed comparing the characteristics shown by the model with experimental results and with several papers. In Chapter 4 all the results are thoroughly explained: the main results that come out of the model for the most general case and all the studies that have been carried out to take advantage of the simulator in order to obtain a better knowledge on the behavior of the machine and how to make it better. Finally the conclusions of the work and the further work that would be done to further improve the simulator are stated in Chapter 5.

Chapter 2

Model description

Contents

As stated in Section 1.2.4 the simulator developed in this work will be used in a machine like the one in Figure 1.8. To understand how the model is obtained, an explanation is required on the theoretical background behind this technology. Once it is properly understood, the model will be presented alongside with the physics behind it.

2.1 Theoretical Background. Autorotation

Autorotation is the physical phenomenon that allows for energy extraction in a rotorcraft. A proper understanding of such phenomenon is needed to build a machine that exploits it for energy harvesting purposes.

The phenomenon of autorotation gained a lot of interest when the first prototypes of helicopters started to be developed. Only some prototypes obtained marginal success and they were not really useful. This changed when Juan de la Cierva realized that it was possible to use autorotation to create a vertical force, replacing the wing of an aircraft. He called his invention the Autogyro. It was the early

1920s. As there was still no engine capable of driving a rotor, the autogyro used a propeller to drive the longitudinal thrust while a non-powered rotor gave the lift to gain altitude. His machine could not achieve neither hover nor vertical flight, but could take-off and land in a fraction of the distance used by common aircrafts [33].

Although the autogyro could not compete with common aircrafts, because of its lack of vertical flight and hover, it pushed forward the research and development of the helicopters. Once the first helicopters succeeded, the research into autogyros and, hence, autorotation, slowed down considerably.

After the first successes of de la Cierva's autogyros, Glauert began the research in this field, establishing the first basics of the theory of the autogyros in his work [34]. This theory was then expanded in the decades of 1920 and 1930 by other researchers such as Lock [35] and Wheatley [36].

Autorotation is the main working principle of the autogyro, but it is key as well for helicopters. They use the autorotation phenomenon in case of engine failure. The rotor stops receiving power from the shaft and thanks to autorotation they descend at a moderate velocity that allows for a safe landing, so it protects helicopters from disaster. A lot of research has been done to study the different autorotating descent regimes of a helicotper, as for example in [33] and [8]. Nowadays the interest in autorotation is resurfacing and several new studies are being made: [37], [10], [38], [39], [7].

While the working behavior of helicopters may seem quite intuitive, autorotation may not. Helicopters create lift with the airflow passing downward through the rotor (see Figure 2.1a) and in autogyros, or autorotation in general, energy is extracted from the incoming flow creating lift with the flow passing upward through the rotor (see Figure 2.1b). That is the reason why when moving forward, the helicopter tilts the rotor forward, while autogyros tilt it backwards.

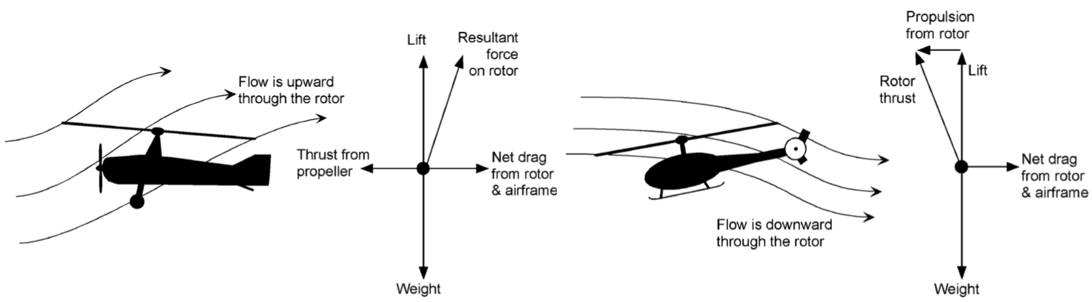

(a) Autogyro flow state (b) Helicopter flow state

Figure 2.1: Rotor tilt, flow direction and overall rotor forces of the autogyro and helicopter. Source [7]

Figure 2.1 shows as well one of the inefficiencies of autogyros. The nature of its backward tilt makes the lift contribute negatively to thrust, requiring more power to generate forward force.

The way in which a rotor in autorotation mode generates lift is the same as for a driven rotor: the rotating blades experience a tangential velocity and, since blade cross-sections are airfoils, they generate aerodynamic lift and drag, variable along the blade. This behavior will be thoroughly studied in Section 2.3.

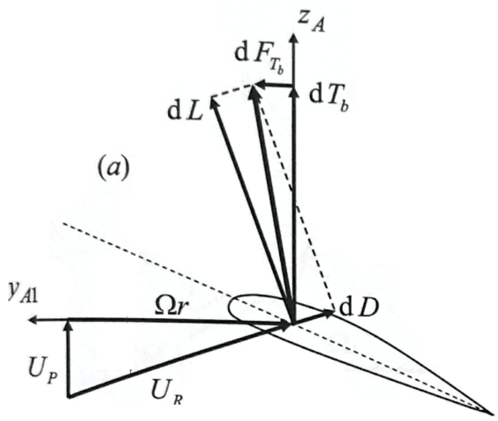

(a) Driving section

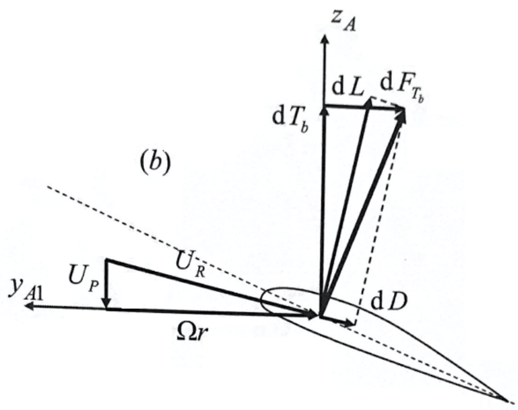

(b) Braking section

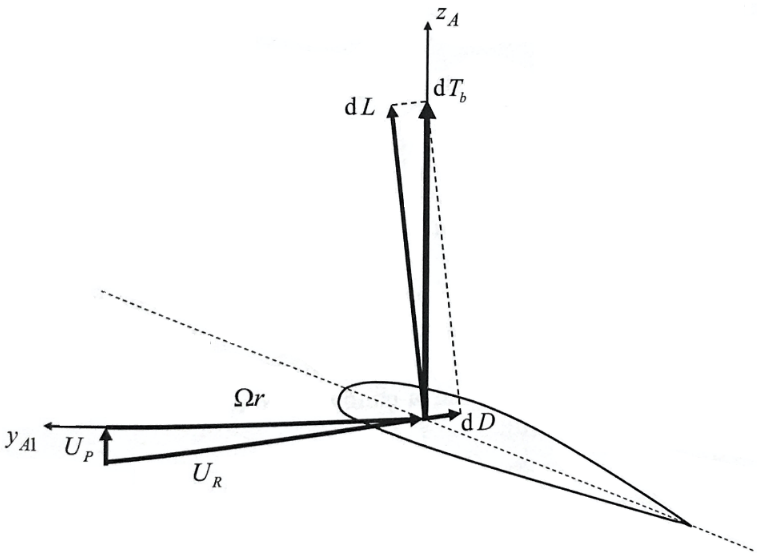

(c) True autorotation section

Figure 2.2: Velocity and aerodynamic forces configurations in three different sections along the same blade. Source [8]

But a first step prior to this analysis would be to understand how the flow going upwards through the rotor makes it rotate. Autorotation in equilibrium is defined as the self-sustained rotation of a rotor where no net torque exists: it does not provide nor extract net energy, so the moment along the shaft M_z is 0 [7]. The turning of the blades in autorotation is caused by the azimuthal asymmetry of the aerodynamic forces along the blade span [8].

Along a given blade, the tangential velocity of any differential section will vary, as this tangential speed will be the result of the product between the rotational speed and the radius of the section. And this is added to a component given by the incoming airflow, that will be equal for all the sections of the blade. The vector addition of this tangential velocity (Ωr in Figure 2.2) and the vertical velocity component of the incoming flow (U_P in Figure 2.2) will have as a result an incidence angle of the flow to the section, or airfoil. And this has a double consequence: first, the angle of attack and the magnitude of the resultant velocity determine the magnitude of the aerodynamic forces, lift (dL) and drag (dD). Second, these aerodynamic forces are defined as lift being perpendicular to the flow direction and drag being parallel to it, so that depending on the angle of attack perceived at each section, not only the magnitude of the forces will change, but also its orientation. And these forces projected into the rotor plane are translated into two different forces: a thrust (dT_b in Figure 2.2), vertical, and a driving force (dF_{T_b} in Figure 2.2) along the y axis that creates a driving moment (tends to accelerate the rotation) or a braking moment (tends to slow down the rotation).

In Figure 2.2 the three different possible states are shown. Figure 2.2a corresponds to a section of a given blade that is generating a positive moment, that tends to accelerate the rotor. In this case, the horizontal (in the rotor-plane reference system) resultant force is positive and, hence, the airfoil is pulled forward, powering the rotation. Figure 2.2b corresponds to a section that is braking the rotation. In this case the resultant horizontal force is backwards, meaning a negative moment that brakes the rotation. Although in Figure 2.2b it is shown a negative incidence angle, this angle may actually be positive or negative, but in any case lower than in the driving sections. Blades in helicopters mainly work in this state. Finally, the section represented in Figure 2.2c is at true autorotation. There is no net horizontal force, meaning that this section doesn't contribute to the rotation, but it still contributes to thrust.

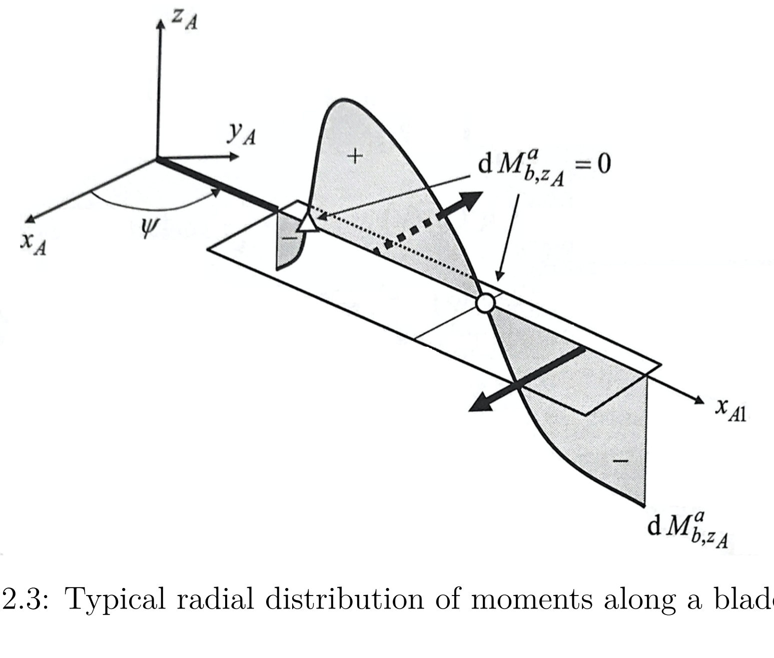

Figure 2.3: Typical radial distribution of moments along a blade. Source [8]

The result is that, along a blade, a radial distribution of moments is obtained, in which some parts of the blade may contribute positively to the rotation and some others negatively, while certain sections may have no contribution. This distribution is related as well to the incidence angle distribution, as it is one of the main variables in the resultant moment of the section. The incidence angle is typically higher at the inward part of the blade and lower at the outward part.

Furthermore, the rotation speed of the rotor will heavily affect the distribution. When the blades rotate at higher angular speeds, the true autorotation sections (sections with zero moment contribution) should move inwards, towards the root.

In autorotation, it is important to take care of the angles of attack (incidence angle plus pitch angle, as explained in Section 2.3) achieved along the blades, as reaching too high angles of attack may cause big portions of the blade to be in stall and cause rapid decreases in lift and decays in the rotational speed.

In Figure 2.3 it can be seen a typical distribution of moments along a blade. The most inward part may typically be in stall due to high incidence angles and low velocities, hence its negative contribution, but once stall is overcome, it begins the driving region. The outward part of the blade contributes negatively. This figure would correspond to a blade with no net rotating moment (positive and negative contributions cancel out). In autorotation (understood as equilibrium autorotation) the sum of the net moments generated by each blade would be zero. However, depending on the characteristics of the problem, the total net moment can be also positive or negative, meaning that the rotor can be accelerating or decelerating towards its equilibrium rotation speed.

This equilibrium point may be stable or unstable, depending on the derivatives of the shaft torque around the equilibrium position, as will be studied in Section 4.2. If it is stable, a perturbation of the equilibrium will generate a moment tending to make the rotor go back to the equilibrium point. If it is unstable, a perturbation will move the rotation state far away from the equilibrium.

Note that Figures 2.2 and 2.3 are reproduced from [8] and the reference system used in these figures is not the same as the one that will be employed to derive the model in the present work.

2.2 KiteRotor and LAKSA

As already stated, the objective of the present work is to develop a dynamic model of an autorotation machine for airborne wind energy applications. The equations of motion correspond to the ones of KiteFlex, a module of the LAKSA software that considers the dynamic and control of a rigid body linked to the Earth by an inelastic and flexible tether [30]. This work will constitute a new module in LAKSA, a lagrangian flight simulator for AWE that does not include RAWE yet. The main novelty included so far, what makes it possible to analyze RAWE instead of the current types of AWE included is the aerodynamic model of the rotor, which presents fundamental differences as compared with a fixed-wing aircraft or a kite. This work follows closely the nomenclature and notation used in [30]. In particular, the gravitational acceleration g, the initial length of the tether length L_0, and the mass of the rotor M_R have been used to normalize the variables.

The tether model is of key importance. For the present work the same model used in all other LAKSA modules is employed. The tether will be divided into several segments, each of them being a straight inelastic rod, and joined together by ideal joints without dissipation. By considering the tether as composed by several rods, flexibility effects in the tether are captured, but elasticity is ignored, which is equivalent as assuming infinite velocity for longitudinal perturbations in the rods [30]. By doing so, fast oscillations are removed and the simulator speed is largely improved.

The tether is attached to the bridle at a point Q and the bridle is attached, in turn, to the rotor, but the tether angles are not allowed to change in this simulator. The rotorcraft will be modeled as a rigid body, and the equations of motion are derived using Lagrange's formalism, not coupled with algebraic constraints. All these aspects of the model are identical to those of [30], so detailed information can be found there.

The state vector of the RAWES dynamic simulator is:

$$\boldsymbol{x}_s = [\gamma_1 \ \ \gamma_2 \cdots \gamma_{N_R} \ \ \varphi_1 \ \ \varphi_2 \cdots \varphi_{N_R} \ \ \theta \ \ \psi \ \ \phi \ \ \lambda_0 \ \ \lambda_c \ \ \lambda_s] \tag{2.1}$$

where N_R is the number of rods used to model the tether, γ_j and φ_j are the angles that define the positions of rod j, and θ, ψ and ϕ are the pitch, yaw and roll angles of the rotor. Finally, the variables λ_0, λ_c and λ_s are the inflow parameters, fully developed in Section 2.3.2. For the analysis of the present work no control has been provided, so there is no control vector. However, the module is prepared to include control variables, in which case the control vector would become:

$$\boldsymbol{x}_c = [\ell_R \ \ \ell_B \ \ \delta \ \ \eta \ \ \theta_1 \ \ \ \theta_2 \cdots \ \theta_{N_b}] \tag{2.2}$$

with ℓ_R the normalized length of a rod, ℓ_B the normalized distance between the center of mass of the rotor and the point Q where the bridle lines and the tether meets, δ and η two angles that define the geometry of the bridle, and θ_{bj} the pitch angle of blade j with j running from 1 to the total number of blades N_b. In our study we will take $\delta = \pi/2$ (point Q is in the line normal to the plane of the rotor passing through its center of mass), and $\eta = 0$ (symmetric bridle). The equations of motion of the system read

$$\frac{d\boldsymbol{x}_s}{d\tau} = \boldsymbol{f}\left(\boldsymbol{x}_s; \boldsymbol{x}_c\right) \tag{2.3}$$

where $\tau = t\sqrt{\frac{g}{L_0}}$ is a dimensionless time.

2.2.1 Kinematic considerations

A tether of length L_0, density ρ_t and cross section A_t connects a fixed point at the ground O_E with the center of mass (point O_B) of a rotor of mass M_R. The rotor has N_b blades of length R and chord c. A reference frame S_{B1} that moves attached to the rotor is defined. It has its origin at O_B, the $\mathrm{x_B}-$axis is along the axis of the blade number 1, and its $\mathrm{z_B}-$axis is normal to the plane of the rotor and points downwards during normal flight. N_b additional frames named S_{B1}, S_{B2}, $\cdots$ S_{Bj} with origin at O_B, $\mathrm{z}-$axis parallel to z_B, and the x-axis along the axis of blades number j will be also used in the analysis (see Figure 2.4). The rotation matrix that relates vector components in the S_{B1} and S_{Bj} frames are

$$\bar{\boldsymbol{R}}_{j1} = \begin{bmatrix} \cos\left(\frac{2(j-1)\pi}{N_b}\right) & \sin\left(\frac{2(j-1)\pi}{N_b}\right) & 0 \\ -\sin\left(\frac{2(j-1)\pi}{N_b}\right) & \cos\left(\frac{2(j-1)\pi}{N_b}\right) & 0 \\ 0 & 0 & 1 \end{bmatrix}. \tag{2.4}$$

The $\mathrm{x}-$axis and $\mathrm{y}-$axis of the body frames span the plane of the rotor. A sketch of the frames of reference is shown in Figure 2.4.

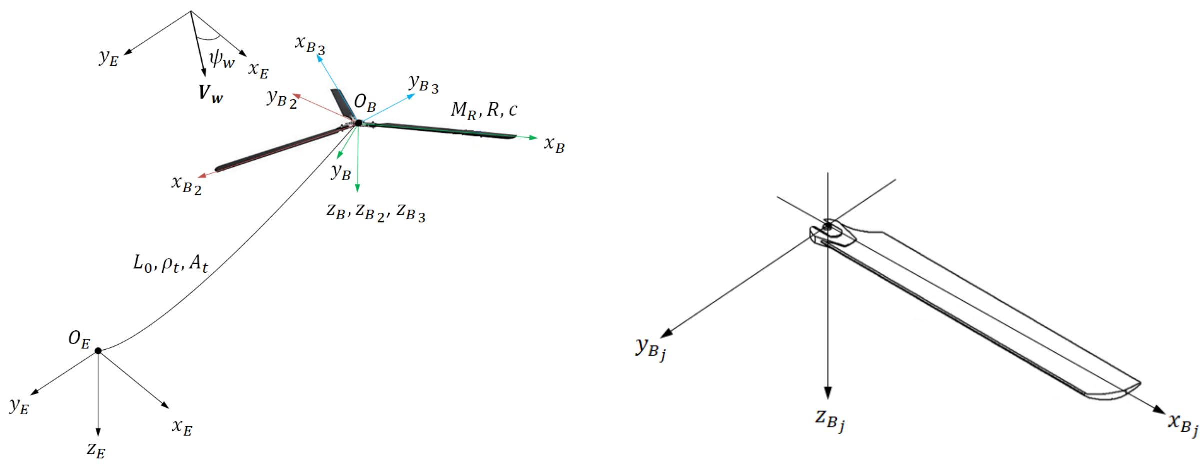

Figure 2.4: Earth and rotor frames of reference (left) and detail of the frame of reference of a blade (right).

Unit vectors along the axes of the frame are denoted by i, j and k and a subscript is added to indicate the frame. For instance, $\mathrm{i_{B1}}, \mathrm{j_{B1}}$ and $\mathrm{k_{B1}}$ are the unit vectors of frame S_{B1}.

The dynamics of the rotor are studied with respect to an inertial frame S_E that has origin at the ground attachment point O_E and its z_E-axis points to the center of the Earth. The wind velocity reads

$$\boldsymbol{V}_w = -\sqrt{gL_0}v_w\left(\cos\psi_w \boldsymbol{i}_E + \sin\psi_w \boldsymbol{j}_E\right) \tag{2.5}$$

where $v_w(t)$ and ψ_w are dimensionless functions that determine the speed and the heading angle of the wind.

Some important kinematic quantities that will appear in the analysis are the angular velocity of the rotor with respect to the inertial frame $\boldsymbol{\Omega}_{BE} \equiv \sqrt{g/L_0}\boldsymbol{\omega}_{BE}$

and the absolute velocity of the center of mass of the rotor $\boldsymbol{V} \equiv \sqrt{gL_0}\boldsymbol{v}$. The normalized aerodynamic velocity of the center of the rotor then reads

$$\boldsymbol{v}_A = \boldsymbol{v} - \boldsymbol{v}_w \ . \tag{2.6}$$

2.2.2 Mass geometry

The rotor that is considered here has the shape of the one shown in Figure 2.4, but it is parametrized so as to rapidly adapt to changes: possible eccentricity of the blades is considered, that is, the beginning of the blades may be at a given distance of the center of rotation. All elements are parametrized so as to account for different number of blades.

One of the rationales behind the potential of AWE is that the outward part of the blades of wind turbines account for the most of the energy generated, so if the kite or glider is used as if it was the outer part of a rotating device, it would be possible to extract most of the energy that could be extracted for a given radius of rotation, but with just a fraction of the mass, besides being possible to obtain a much bigger radius. The same reasoning is expected to be applied for RAWES. As it was explained in Section 2.1, the inward parts of the blades may be typically in stall, and even if they are not, they will account for a small contribution. That is why it is expected for these machines to have the blades separated from the center of rotation, making possible to obtain greater radius and surface but with limited mass. However, structural constraints may make this not possible.

In the case where the blades do not meet at the center of rotation, it is considered that they are attached at the center of rotation through rods of a given mass and constant density and cross-section.

The center of mass of the rotor coincides with point O_B. The tensor of inertia of the rotor will have great effect in its behavior. The components of the tensor of inertia with respect to the body axes are generalized for a rotor of N_b blades. It will be obtained very easy by using the following properties:

- $I_x = I_y$ due to symmetry.
- Consider the property:

$$I_x + I_y + I_z = 2I_0 \tag{2.7}$$

  where I_0 is the inertia calculated with respect of the point where the three orthogonal axis meet, O_B in the S_{B1} frame, and that, since there is no mass out of the $x - y$ plane, will be equal to I_z.

Thanks to these relations it is only necessary to calculate I_z. Let R_{hub} be the radius of the hub of the rotor, that is, the distance from the center of rotation to the beginning of the blade. Let L_{blade} be the length of the blade. Then, the moment of inertia with respect to the central point, reads:

$$I_0 = I_z = N_b \cdot \int_m (x^2 + y^2)\ dm\ . \tag{2.8}$$

The moment of inertia of only one blade can then be calculated with respect to the central point. Let this blade be the one coinciding with the body x axis. Assuming that the mass is concentrated along a line, the moment of inertia can be integrated assuming two different constant densities along this line: $\rho_1 = m_1/R_{hub}$ for $x \in [0, R_{hub}]$ and $\rho_2 = m_b/L_{blade}$ for $x \in [R_{hub}, R]$, where $R = R_{hub} + L_{blade}$ is the total radius of the rotor, and being m_1 the mass of the cable attaching the center of the rotor to the blade, and m_b the mass of the blade itself, so that the total mass of the rotor will be:

$$M_R = N_b(m_1 + m_b)\ . \tag{2.9}$$

Then the moment of inertia with respect to the center point is:

$$I_0 = I_z = N_b \cdot \int_m (x^2)\ dm = N_b \cdot \left(\rho_1 \int_0^{R_{hub}} x^2 dx + \rho_2 \int_{R_{hub}}^{R} x^2 dx \right) \tag{2.10}$$

$$= N_b \cdot \left(\frac{R_{hub}^3}{3} \left(\frac{m_1}{R_{hub}} - \frac{m_b}{L_{blade}} \right) + \frac{m_b}{L_{blade}} \frac{R^3}{3} \right)\ . \tag{2.11}$$

Knowing I_z then it is straight forward to obtain I_x and I_y, which are:

$$I_x = I_y = \frac{N_b}{2} \cdot \left(\frac{R_{hub}^3}{3} \left(\frac{m_1}{R_{hub}} - \frac{m_b}{L_{blade}} \right) + \frac{m_b}{L_{blade}} \frac{R^3}{3} \right)\ . \tag{2.12}$$

2.3 Aerodynamic modelization

Several types of rotors exist, depending on their degrees of freedom. In the present work a rigid rotor is considered, with no flapping and lagging movements allowed. Early prototypes made in this field are typically of this type, because it is the simplest and cheapest form. However, the flapping and lagging movements improve a lot the behavior of the rotor, making it easier to control and reducing vibrations. However, although not having hinges to allow for flapping motion, the natural flexibility of the blades can also be substituted for the presence of hinges, as is for instance the case in hingeless helicopter rotors. This will not be modeled in the present work, while real prototypes and machines will experience it.

The dynamic simulator will need at each time step the aerodynamic forces and moments that the rotor is generating, in order to integrate the equations of motion and calculate all the variables at the following time step. Typical research done with autogyros, such as [34], [36], [35] and also new ones as it is the case of [31] calculate these forces and moments based on a combination of Glauert's momentum theory with Blade Element Theory (BET) to calculate forces and moments along the blade and then integrate over one revolution.

This approach is very useful when trying to make steady analysis. However for the dynamic simulator being developed here that is not possible. To simulate the movement of the blades and the whole rotor at each time step with precision the integral over one rotation is not feasible, because a much smaller time step must be used in order to obtain the effect of instantaneous forces and moments. For example, the pitching moment may be zero when performing the one-revolution calculation, but, in reality, at a given instant during the revolution the pitching moment may be high, provoking the movement of the rotor and changing the aerodynamic variables in successive time steps, changes that would not be taken into account in the one-revolution approach. For that reason, the forces and moments will be obtained by applying directly Blade Element Theory. Applying BET to a rigid rotor is much easier than for an articulated one and yet it brings up the most important characteristics of the aerodynamics of the rotor [8].

While BET will be used for modeling the aerodynamic forces and moments, a dynamic inflow model will be needed to properly estimate the aerodynamic velocity experienced at each section of the blades. The dynamic inflow model is able to obtain a map of the actual induced velocity experienced at each point of the rotor, hence being much more close to reality than a model that takes a constant induced velocity in every point of the rotor. Furthermore, it is dynamic, so the induced velocity at each time step will depend on the forces and moments and also on the inflow state at the previous time step. This result of the inflow model at each time step will be an input for the BET, so both are highly related. For the inflow model, the Pitt & Peters approach will be implemented.

2.3.1 Blade Element Theory

Blade Element Theory is, as defined by [8]: "The simplest theory that allows to use geometric and construction parameters of the rotor as it is the case of the airfoil, chord, span, torsion and number of blades". It consists in dividing the blade span into infinitesimal sections, which will be airfoils, and calculate the aerodynamic forces of the airfoil, as well as their contribution to the moment with respect to the rotation center. Then they are integrated along the blade to obtain the instant forces and moments generated by each blade.

Therefore, to apply that, all the aerodynamic characteristics must be assessed at each infinitesimal section.

The pitch angle $\theta_{bj}(t)$ of blade j is defined as the angle between its zero-lift-line and the plane of the rotor, as can be seen in Figure 2.5. This angle is a control variable. The normalized aerodynamic velocity of a section of blade j located at distance $r = R\tilde{r}$ from the center of the rotor will be the addition of three different contributions: the aerodynamic velocity of the rotor (sum of incoming wind and rotor displacement velocity), the tangential velocity generated from the rotation, and the induction velocity:

$$\boldsymbol{v}_{Aj}(\tilde{r}) = \boldsymbol{v}_A + \tilde{R}\boldsymbol{\omega}_{BE} \times \tilde{r}\boldsymbol{i}_{Bj} - v_i\,\mathbf{k}_{Bj} \tag{2.13}$$

with $\tilde{R} = R/L_0$ and $r_{blade} < \tilde{r} < r_{max}$. The radius r_{max} is used instead of 1 to account for blade tip losses, a phenomenon that has been widely acknowledged. The value chosen is $r_{max} = 0.97$, meaning that the last 3% of the blade should not be taken into account. This value was first proposed by Glauert [34] and has been used as reference ever since. This effect happens because at the blade tip there appears some recirculating flow, which generates a drop in the angle of attack that finally results in no generation of lift. To counteract this, helicopters may use special shapes for the blade tip, such as swept blade tips.

The reality is not as sharp as cutting the aerodynamic forces at 97% of the blade span. The lift generated by the blade in the tip evolves smoothly to get to 0 at the tip, but getting rid of the last 3% has been seen to reproduce this effect accurately enough and very simply.

The fact that the blades start at a certain distance affects the force and moment calculations. Let r_{blade} be the position at which the blade begins, as a fraction of the total rotor radius, this is:

$$r_{blade} = \frac{R_{hub}}{R_{hub} + L_{blade}} \; . \tag{2.14}$$

Finally, $v_i\,\mathbf{k}_{Bj}$ in Equation 2.20 is the axial induced velocity correction, further detailed in Section 2.3.2.

The lift coefficient $C_{Lr}(\alpha_{rj})$ and drag coefficient $C_{Dr}(\alpha_{rj})$ of a section of blade j depend on its local angle of attack (see left panel in Figure 2.5). The angle of attack will be the sum of the pitch angle θ_{bj} and the incidence angle φ_{rj}. The incidence angle is determined only by the direction of the resultant aerodynamic velocity of the section, regardless of its pitch angle. It will depend on the $\boldsymbol{j}$ and $\boldsymbol{k}$ components of the velocity, that is, the velocity component along the blade span does not contribute to the incidence angle. Therefore, a higher proportion of tangential velocity would result in a lower incidence angle, and a negative vertical velocity would result in a negative incidence angle. With that, the angles of attack and incidence read

$$\alpha_{rj} = \theta_{bj}(t) + \varphi_{rj}, \qquad \varphi_{rj} \equiv \arctan\left[\frac{\boldsymbol{v}_{Aj}(\tilde{r}) \cdot \boldsymbol{k}_{Bj}}{\boldsymbol{v}_{Aj}(\tilde{r}) \cdot \boldsymbol{j}_{Bj}}\right] \; . \tag{2.15}$$

Therefore, the total normalized aerodynamic force is

$$\begin{aligned} \boldsymbol{f}_A \equiv \frac{\boldsymbol{F}_A}{M_R g} = \chi \sum_{j=1}^{N_b} \int_{r_{blade}}^{r_{max}} \boldsymbol{v}_{Aj}^2(\tilde{r}) \,[C_{Lr}(\alpha_{rj})\,(\sin\varphi_{rj}\boldsymbol{j}_{Bj} - \cos\varphi_{rj}\boldsymbol{k}_{Bj}) \\ - C_{Dr}(\alpha_{rj})\,(\cos\varphi_{rj}\boldsymbol{j}_{Bj} + \sin\varphi_{rj}\boldsymbol{k}_{Bj})]\, d\tilde{r} \; , \end{aligned} \tag{2.16}$$

while the total normalized aerodynamic moment is

$$\boldsymbol{m}_A \equiv \frac{\boldsymbol{M}_A}{M_R g L_0} = \chi \tilde{R} \sum_{j=1}^{N_b} \int_{r_{blade}}^{r_{max}} \boldsymbol{v}_{Aj}^2(\tilde{r}) \left[C_{Lr}(\alpha_{rj}) \left(\sin\varphi_{rj} \boldsymbol{k}_{Bj} + \cos\varphi_{rj} \boldsymbol{j}_{Bj} \right) \right.$$
$$\left. - C_{Dr}(\alpha_{rj}) \left(\cos\varphi_{rj} \boldsymbol{k}_{Bj} - \sin\varphi_{rj} \boldsymbol{j}_{Bj} \right) \right] \tilde{r} d\tilde{r} \ . \tag{2.17}$$

Our model uses the lift and drag coefficients of an airfoil NACA 0015 at $Re = 2 \times 10^6$ [40]. The airfoil selection has been based on several reasons. In the past, helicopters used mainly symmetrical airfoils for their blades, providing a good behavior regarding maximum lift coefficient while producing low values of pitching moment [8]. However, some benefits can be obtained when adding camber to the airfoil, providing a smoother shape at the leading edge, attaining higher values of maximum lift coefficient. But, in the end, the NACA symmetrical airfoil was thought to be a better compromise, as it will also allow to have a better understanding of the effect of increasing the collective pitch. Finally, among the NACA symmetrical airfoils, thickness to chord ratios around 12% are recommended [8] and the NACA 0015, although showing a slightly higher thickness to chord ratio, it shows a very similar behavior and data was found on its lift and drag coefficients for angles ranging from 0º to 180º in [40]. The right panel in Figure 2.5 shows the lift and drag coefficients versus the angle of attack, where the values from 180º to 360º have been obtained by symmetry.

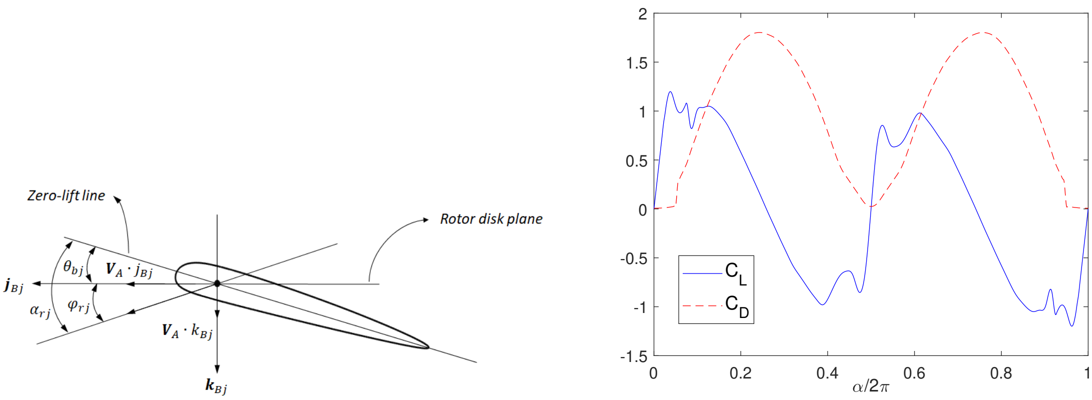

Figure 2.5: Definition of the angles in a section of a blade (left) and lift and drag coefficients versus the angles of attack (right) .

2.3.2 Inflow model

The inflow model used in the simulator was first developed by Pitt & Peters. Their dynamic inflow model allows to take into account the unsteady dynamics of the wake developing downstream of the rotor, which depends on the blade's rotation and the overall thrust generated by the rotor. These aerodynamic loads are indeed influenced by the dynamic inflow, so these two modules should be feeding one another so that the model forms a closed loop.

Notation

The components of the aerodynamic velocity **V** (farfield wind plus craft velocity) seen in a body frame, different from the one used until now, attached to the hub of the rotor and rotating, are noted V_x, V_y, V_z. We also note $V = \sqrt{V_x^2 + V_y^2}$ the velocity magnitude in the rotor plane. Note that this magnitude will remain the same no matter how the body frame is set, as long as the z axis is perpendicular to the rotor plane, so the rotating body frame is not an issue.

However, everything will be calculated in non-dimensional form. To ensure continuity with the rest of the modules in LAKSA, the velocity will be non-dimensionalized using the same convention of LAKSA. Hence, the velocity called V will be made non-dimensional as:

$$v = \sqrt{v_x^2 + v_y^2} \tag{2.18}$$

The same is applied to the angular velocity of the rotor with respect to the inertial frame and the dimensionless time ($\tau = t\sqrt{\frac{g}{L_0}}$).

The axial induced velocity field over the rotor disk is assumed to vary as follows:

$$v_i(\tilde{r}, \psi, t) = v_0(t) + v_s(t)\,\tilde{r}\sin\psi + v_c(t)\,\tilde{r}\cos\psi, \tag{2.19}$$

where $\tilde{r}$ is the radial coordinate, and ψ the azimuth. The azimuth is set to $\psi = 0°$ in the direction of incoming flow if the rotor is assumed as fixed, or equally, in the opposite direction of the aerodynamic velocity of the rotor as seen from the rotor. Then the azimuth is set positive clockwise starting from this $\psi = 0°$, as shown in Figure 2.6.

The aerodynamic loads are calculated by first integrating along the blade the resultant loads at a differential blade section, and then summing the result of all the blades. Then, the normalized aerodynamic velocity of a section of blade j located at distance $r = R\tilde{r}$ from the center of the rotor is, recovering the notation of our model:

$$\boldsymbol{v}_{Aj}(\tilde{r}) = \boldsymbol{v}_A + \tilde{R}\boldsymbol{\omega}_{BE} \times \tilde{r}\boldsymbol{i}_{Bj} - v_i\,\mathbf{k}_{Bj} \tag{2.20}$$

with $\tilde{R} = R/L_0$, $r_{blade} < \tilde{r} < r_{max}$ and ω_{BE} the non-dimensional angular velocity of the rotor with respect to the inertial frame, while $v_i\,\mathbf{k}_{Bj}$ is the axial induced velocity correction.

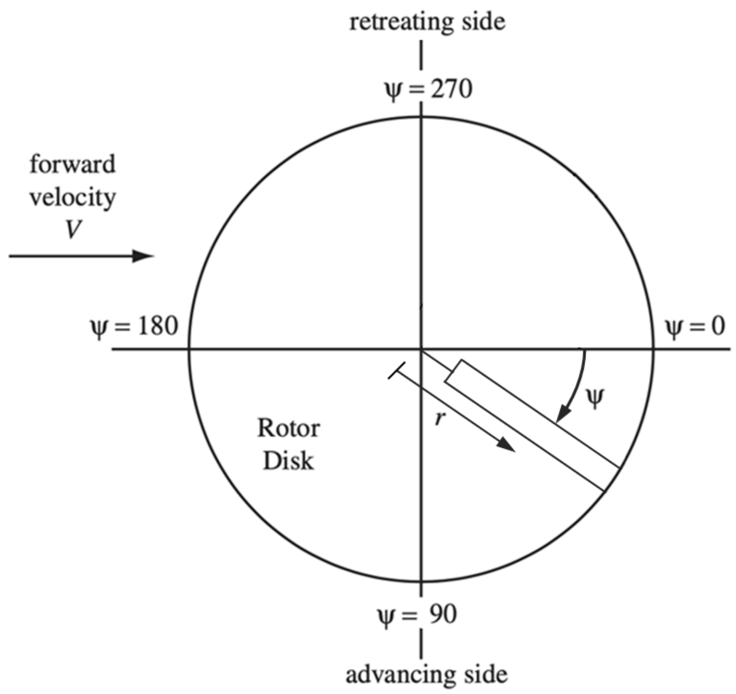

Figure 2.6: Azimuth convention to be used

Pitt & Peters dynamic inflow model

The working scheme of the Pitt & Peters dynamic inflow model is shown in Figure 2.7.

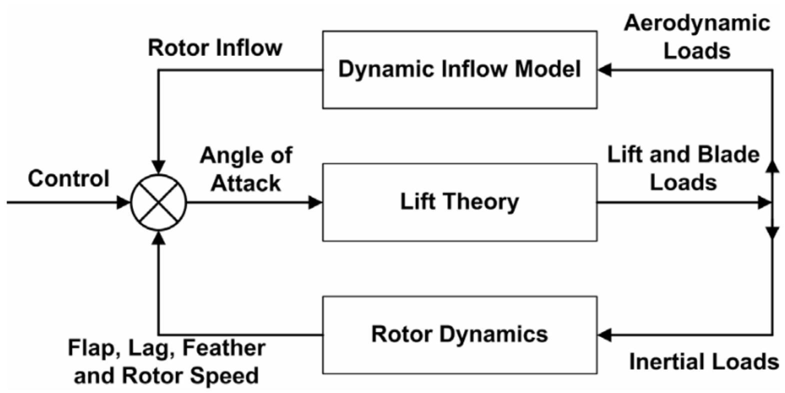

Figure 2.7: Block diagram schematic of the inflow dynamic model [9]

The model by [41] is established in a set of axes aligned with the projection of the aerodynamic velocity in the rotor plane as shown in Figure 2.8.

It should be noted that, even if Johnson's reference frame is such that positive z-axis is pointing upwards, the induced velocity is taken as positive when directed

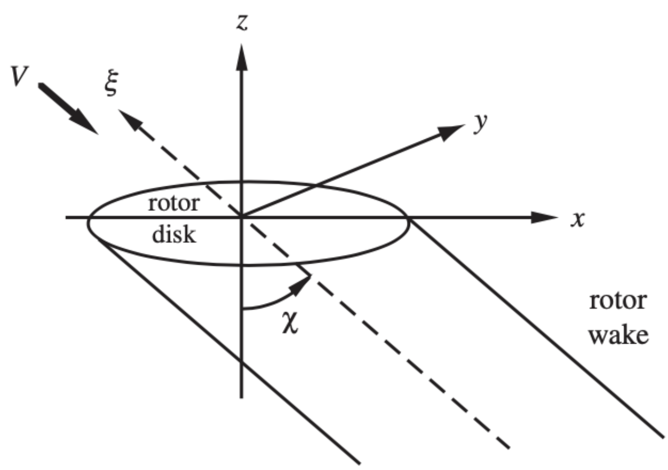

Figure 2.8: Johnson's reference frame

downwards. Hence, a positive induced velocity will mean that the flow is slowed down when passing through the rotor, as it should in autorotation.

In our model the forces and moments are calculated in body axis, so a transformation matrix **P** will be used to transform the body frame into the velocity frame such that

$$\begin{bmatrix} C_T \\ C_{M_y} \\ C_{M_x} \end{bmatrix}^w = \mathbf{P} \begin{bmatrix} C_T \\ C_{M_y} \\ C_{M_x} \end{bmatrix} . \tag{2.21}$$

On the right-hand side, the components are expressed in the body frame. On the left-hand side, the superscript w indicates that the components of the induced velocity are expressed in the frame aligned with the aerodynamic velocity. This matrix **P** will be of the form:

$$\mathbf{P} = \begin{bmatrix} \cos\phi & -\sin\phi & 0 \\ -\sin\phi & -\cos\phi & 0 \\ 0 & 0 & -1 \end{bmatrix} \tag{2.22}$$

where a double rotation is performed. First, a rotation around the $\mathbf{k_b}$ axis of an angle ϕ, which is the angle formed between the $\mathbf{i_b}$ axis and the projection vector of the aerodynamic velocity on the rotor plane. Then, a rotation of 180º around the resultant x-axis.

To obtain the angle ϕ, the aerodynamic velocity of the rotor in the body frame is used. This velocity has two components in the rotor plane and one perpendicular to it. Therefore, the first step is to calculate the angle formed by the aerodynamic velocity vector in the 2D rotor plane (its [x,y] components) and the body frame x-axis. Then, the angle searched is the one calculated plus 180º, since the convention used by [33] shows an x-axis aligned with the incoming flow vector, that is, as assuming the aircraft fixed and the wind in motion.

The dynamical equations of the Pitts & Peters model that will be used here, describing the 3-states model are the ones proposed by [33]:

$$\mathbf{LM}\frac{\mathrm{d}}{\mathrm{d}\tau_J}\begin{bmatrix}\lambda_0\\ \lambda_c\\ \lambda_s\end{bmatrix}^w + \begin{bmatrix}\lambda_0\\ \lambda_c\\ \lambda_s\end{bmatrix}^w = \mathbf{L}\begin{bmatrix}C_T\\ -C_{M_y}\\ C_{M_x}\end{bmatrix} \tag{2.23}$$

where the dynamic integration is made with τ_J, which is the non-dimensional time used in Johnson's book [33] (non-dimensionalized using Ω). C_T is the thrust coefficient, C_{M_y} the pitch moment coefficient, and C_{M_x} the roll moment coefficient, all of them computed in Johnson's frame [33]. It is important to note that in Equation 2.23 everything is non-dimensionalized with Johnson's [33] parameters. Therefore, the variables under the symbol λ (λ_0, λ_c, λ_s) correspond to the induced flow parameters of Equation 2.19 but, instead of being non-dimensinalized using the LAKSA convention (Equation 2.19 uses this convention), dimensional velocity V is non-dimensionalized as follows:

$$v = \frac{V}{\sqrt{gL_0}} \qquad \Rightarrow \qquad \lambda = \frac{V}{\Omega R} \ . \tag{2.24}$$

However, the calculation of the forces and moments must include the induced velocity with the non-dimensionalization of this work. Hence, they are easily related as:

$$v = \lambda \cdot \omega \tilde{R} \tag{2.25}$$

being Ω and ω the magnitude of the rotor's angular speed in dimensional and non-dimensional form respectively. To include these dynamic Equation (2.23) in LAKSA, the induced flow parameters will be included in the state vector. But these equations are integrated with an non-dimensional time:

$$\tau_J = t \cdot \Omega \ . \tag{2.26}$$

Then, we relate both derivatives applying the chain rule:

$$\frac{d\lambda}{d\tau_J} = \frac{d\lambda}{d\tau} \cdot \frac{1}{\omega} \ . \tag{2.27}$$

The thrust and moment coefficients are Johnson's [33] non-dimensional variables, this is:

$$C_T = \frac{T}{\rho\pi R^4\Omega^2} \quad , \qquad C_M = \frac{M}{\rho\pi R^5\Omega^2} \ . \tag{2.28}$$

To obtain them, the force and moment vectors are rotated to the wind axis, by using matrix $\boldsymbol{P}$. Then, the coefficients are obtained as:

$$C_T = \Gamma \cdot \frac{f_{A_z}}{\tilde{R}^4 \omega^2} \quad , \quad C_{M_y} = \Gamma \cdot \frac{m_{A_y}}{\tilde{R}^5 \omega^2} \quad , \quad C_{M_x} = \Gamma \cdot \frac{m_{A_x}}{\tilde{R}^5 \omega^2} \tag{2.29}$$

being,

$$\Gamma = \frac{M_R}{\rho \pi L_0^3} \ . \tag{2.30}$$

The matrices **L** and **M** read as follows [33],

$$\mathbf{M} = \begin{bmatrix} \frac{128}{75\pi} & 0 & 0 \\ 0 & \frac{64}{45\pi} & 0 \\ 0 & 0 & \frac{64}{45\pi} \end{bmatrix} \tag{2.31}$$

and

$$\mathbf{L} = \begin{bmatrix} \frac{1}{2v_t} & -\frac{15\pi}{64 v_m}\sqrt{\frac{1-\cos\chi}{1+\cos\chi}} & 0 \\ \frac{15\pi}{64 v_t}\sqrt{\frac{1-\cos\chi}{1+\cos\chi}} & \frac{4\cos\chi}{v_m(1+\cos\chi)} & 0 \\ 0 & 0 & \frac{4}{v_m(1+\cos\chi)} \end{bmatrix} \ . \tag{2.32}$$

In matrix L two effective velocity terms are used. Through momentum theory a given expression for the mean induced velocity is obtained, and it is observed to be valid for some cases. However, [33], [9] and [39] agree that, for the flow terms, it should be substituted by a mass-flow parameter obtained through differential momentum theory to give a more precise distribution of induced velocity for either ascent or descent flight, implying that the terms used in Equation 2.32 are:

$$v_t = \sqrt{\mu^2 + \bar{\lambda}^2} \ , \tag{2.33}$$

$$v_m = \frac{\mu^2 + \bar{\lambda}\left(\bar{\lambda} + \lambda_i\right)}{\sqrt{\mu^2 + \bar{\lambda}^2}} \ . \tag{2.34}$$

The Pitt & Peters equations were initially established for helicopters, and were then adapted for autorotation by Houston ([38], [42], [10] and [37]). The equations themselves remain the same (Equation 2.23), but Houston's convention will be used for defining the parameters in v_t and v_m [37]:

$$\mu = \frac{V_{plane}}{\Omega R} \equiv \frac{v_{plane}}{\omega \tilde{R}} \ , \tag{2.35}$$

$$\mu_z = \frac{V_{out}}{\Omega R} \equiv \frac{v_{plane}}{\omega \tilde{R}} \ , \tag{2.36}$$

where V_{plane} and V_{out} are the rotor plane and out-of-rotor plane velocity magnitude respectively, with the lower case velocities being those non-dimensionalized with the present work convention. Note that μ_z is defined positive when the airflow goes through the rotor upwards.

Then, χ is the wake skew angle, computed as

$$\cos\chi = \frac{\left|\bar{\lambda}\right|}{\sqrt{\mu^2+\bar{\lambda}^2}} \ . \tag{2.37}$$

Finally,

$$\lambda_i = \frac{C_T}{2\cdot\sqrt{\mu^2+\bar{\lambda}^2}} \tag{2.38}$$

$$\bar{\lambda} = \lambda_i - \mu_z \ . \tag{2.39}$$

Note that Equations 2.38 and 2.39 are coupled, so a Newton method will be applied at each time-step to obtain these two parameters. The iterative Newton-Raphson method proposed by Johnson [33] is chosen for implementation. It solves for $\bar{\lambda}$:

$$\hat{\lambda}_{in} = \frac{\lambda_h^2}{\sqrt{\bar{\lambda}_n^2+\mu^2}} \ , \tag{2.40}$$

$$\bar{\lambda}_{n+1} = \bar{\lambda}_n - \frac{\bar{\lambda}_n - \mu_z - \hat{\lambda}_{in}}{1+\hat{\lambda}_{in}\bar{\lambda}_n/(\bar{\lambda}_n^2+\mu^2}f \tag{2.41}$$

where $\lambda_h^2 = C_T/2$ and a relaxation factor of $f = 0.5$ is used to improve convergence [33]. In order to initialize the solution, the first guess will be:

$$\bar{\lambda} = \frac{\lambda_h^2}{\sqrt{(\lambda_h+\mu_z)^2+\mu^2}} \ . \tag{2.42}$$

However, care should be taken because this method is developed with Johnson's convention for μ_z, which is different from the one used in the present work, so μ_z should change sign when performing this Newton-Raphson iteration method.

2.4 Force exerted by the anchor kite

Some early prototypes of RAWES that do not incorporate active control typically include elements such as kites or balloons to confer improved stability to the machine, as [43] and [4] did. The configuration that is going to be used to analyze results in order to validate our model will be the one by Christof Beaupoil [4], which uses a kite for stabilization. See in Figure 3.1 the machine itself.

This kite acts as a kind of anchor in the sky, attached to the rotor and that tends to keep it in its position. To model the effect of the kite, it will be considered a force acting on the rotor center, perpendicular to the rotor plane in the stable position of Figure 2.9, and modeled as a spring and damper, hence proportional to the elongation and elongation rate of the cable connecting the rotor and the kite. This will be modeled by taking into account the position at which the machine is seen to stabilize (see Figure 2.9), as it can be followed hereunder.

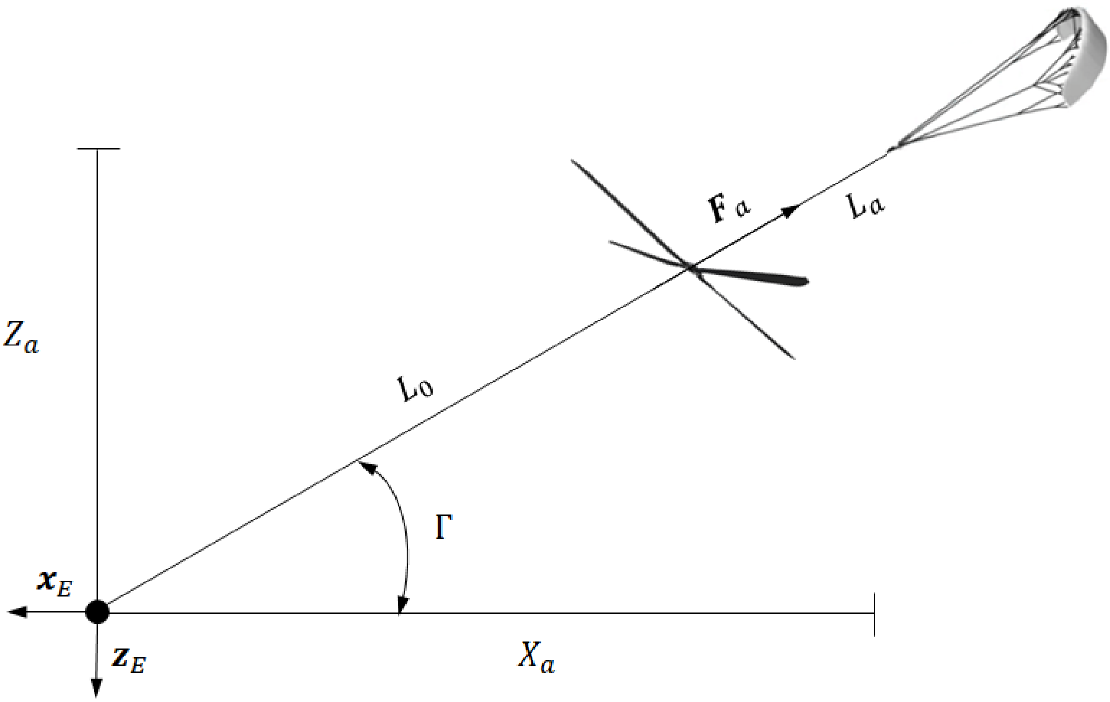

Figure 2.9: Stable situation of the machine.

The position of the kite will be considered as fixed, in the same direction as the tether (in the experimentally observed equilibrium position), and at a distance L_a (a coming from *anchor*) of the rotor. The angle formed between the tether and the ground will be called Γ. We can then obtain the position of the kite as:

$$X_a = -(L_0 + L_a) \cdot \cos(\Gamma) \tag{2.43}$$

$$Z_a = -(L_0 + L_a) \cdot \sin(\Gamma) \; . \tag{2.44}$$

Then, the position vector of the kite:

$$\boldsymbol{r_a} = \frac{X_a}{L_0}\boldsymbol{i_E} + \frac{Z_a}{L_0}\boldsymbol{k_E} \; . \tag{2.45}$$

Let's define $\boldsymbol{r}$ as the vector going from the center of mass of the kite ($\boldsymbol{r_k}$) to the center of mass of the anchor ($\boldsymbol{r_a}$):

$$\boldsymbol{r} = \boldsymbol{r_a} - \boldsymbol{r_k} \ . \tag{2.46}$$

The actual distance between rotor and kite may vary, so let its magnitude be, taking into account that the position vectors are non-dimensionalized with the tether length L_0, the difference between the actual length ($|\boldsymbol{r}|$) and the "natural length of the spring" (L_a):

$$\epsilon = |\boldsymbol{r}| - \frac{L_a}{L_0} \ . \tag{2.47}$$

while the elongation rate, $\dot{\epsilon}$ is:

$$\dot{\epsilon} = \frac{d\epsilon}{d\tau} = \frac{\boldsymbol{r} \cdot \boldsymbol{v_k}}{|\boldsymbol{r}|} \tag{2.48}$$

and the force is exerted in the direction of the cable pointing to the kite, this is:

$$\boldsymbol{u} = \frac{\boldsymbol{r}}{|\boldsymbol{r}|} \tag{2.49}$$

Finally, k_0 (N/m) being the spring constant and ξ (Ns/m) the damper constant, the force exerted by the kite:

$$\boldsymbol{f_a} = \frac{\boldsymbol{F_a}}{M_R g} = \frac{L_0}{M_R g}\left(k_0 \cdot \epsilon + \xi\sqrt{\frac{g}{L_0}} \cdot \dot{\epsilon}\right)\boldsymbol{u} \equiv \left(\tilde{k_0}\epsilon + \tilde{\xi}\dot{\epsilon}\right)\boldsymbol{u} \ . \tag{2.50}$$

2.5 Energy extraction

Several ways exist to extract energy from the machine in a ground-based manner. To be able to compare the energy extracted with real data, the configuration of the machine, as already stated, will be the one by Christof Beaupoil [4], so its energy extraction system will be mimicked.

It is a ground generation RAWES that is able to extract energy from the air by transmitting torsion from the rotor to ground. This transmission is made possible thanks to the a structure called Open Tensegrity Shaft (hereafter called OTS for simplicity). It is a strucutre that substitutes the simple tethers used in other cases. The OTS is "a rotating three-dimensional long structure made of components in compression (struts) and tension (tethers) for the torsion based transmission of power" [4].

This structure is very well fitted to transmit torsion, so it rotates with the rotor and drives a wheel that is in charge of generating electricity. Furthermore, because the structure is still a prototype and, therefore, not thought to be as stiff as possible, the experiments have concluded that the machine should not be allowed to rotate at more than 115 *rpm*, otherwise it will break. Therefore, the wheel at the other end of the OTS will provide variable friction to cut-off the rotation speed of the rotor to 115 *rpm*. This variable friction is regulated through a PID, so to simulate this behavior, a PID has been implemented in the model.

This PID is set to be a proportional PID, whose constant has been set to $PID = -0.1$. The implementation of this PID is done by adding a moment and a generalized force. Therefore, the moment extracted from the machine will be:

$$\epsilon = |\omega_{BE}| - \omega_{targ} \tag{2.51}$$

$$M_{rev} = PID \cdot \epsilon \cdot \boldsymbol{k_{Bj}} \tag{2.52}$$

being $\omega_{targ} = 115$ *rpm* is the target rotation speed, to be used in non-dimensional form.

This moment M_{rev} will be actually the moment that is extracted from the machine and that drives the electicity generation wheel.

Chapter 3

Verification and validation

Contents

Verification and validation are two key concepts in the development of any type of software. If the system or code is not verified or validated, one may be trusting results and acting upon them, and the results be far away from the reality. Therefore, before getting any useful output from the built dynamic simulator a process of verification and validation will be carried out, and only after doing so, results can be obtained.

The present system is a modification and extension of LAKSA, which was already verified and validated [30]. Therefore, the efforts should focus in validating and verifying the modules developed in this work and implemented within LAKSA. These modules are the whole aerodynamic module and a subsystem of it, the induction model.

	Houston [10]	**Simulation**
Max. induced speed λ	0.043	0.045

Table 3.1: Inflow result comparison with [10]

Two main validations have been carried out, one regarding the inflow model and one regarding the whole aerodynamic module. Results can be easily found in Tables 3.1 and 3.2 respectively. More insight will be given on these results in their corresponding sections: 3.2 and 3.3. But before getting into that, the geometry used will be commented upon.

	Christof [4]	Sim. at 5.7 m/s	Sim. at 4 m/s
Extracted moment $\lvert M_z \rvert$ (Nm)	3.75	9.85	4.25
Lift force N	200	82	44

Table 3.2: Aerodynamic comparison with [4]

3.1 Geometry

The validation of the simulator will be performed by comparison with the results obtained by Christof Beaupoil with his prototype.

This machine complies with all the geometrical constraints for which the model has been developed. It is a rotor composed of 4 blades, being the blades displaced from the rotation center, and the energy is generated in ground thanks to the torsion transmitted from rotor to ground station through the OTS structure. The machine is shown in Figure 3.1.

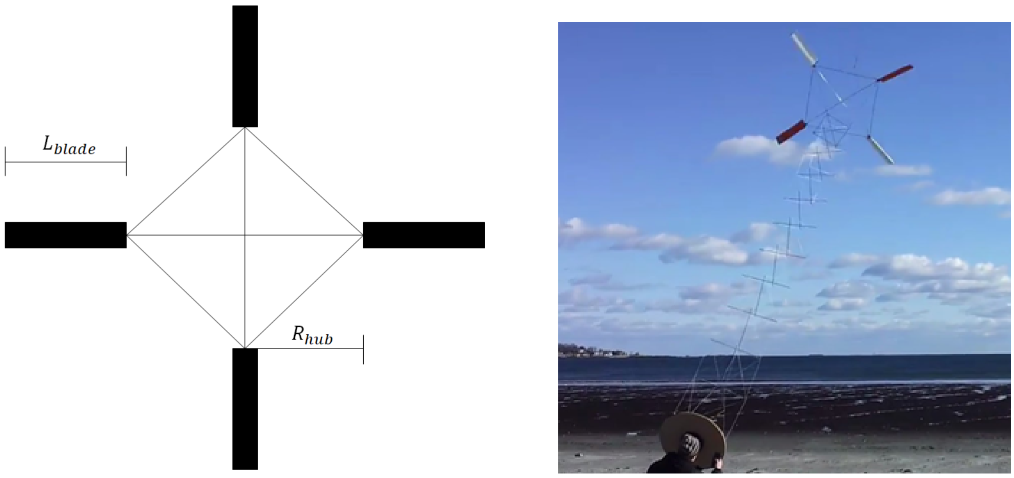

Figure 3.1: Ground generation RAWES sketch (left) and real machine attached by the OTS (right) [4] .

However, the OTS structure is not modeled. Instead, our model will keep being attached by a thin tether, so the inertial effects of the torsion of the OTS structure will not be taken into account.

3.2 Inflow model

To validate the implementation of the dynamic inflow model, mainly two papers have been used. The first is the study made by S.S. Houston in [37] in which they compare experimental results of a an autogyro with the results using an inflow model as the one described here. The main result that it can be extracted from this paper is the fact that Houston obtains, as he expected, an inflow distribution such that the maximum downwash velocity obtained in the rotor should be located in the back of the rotor, while in the front of the rotor the least downwash is expected, being possible to even obtain some upwash depending on the conditions of the autorotation. Then the rest of the rotor evolves smoothly from maximum to minimum downwash.

To check whether this behavior is observed, the rotor disk has been plotted and colormapped by the non-dimensional induced velocity λ in Figure 3.2. It is checked then if the behavior observed by Houston is reproduced in our rotor (note that the front is referred to the part where the wind is coming from, hence at $\psi = 180^{\text{o}}$).

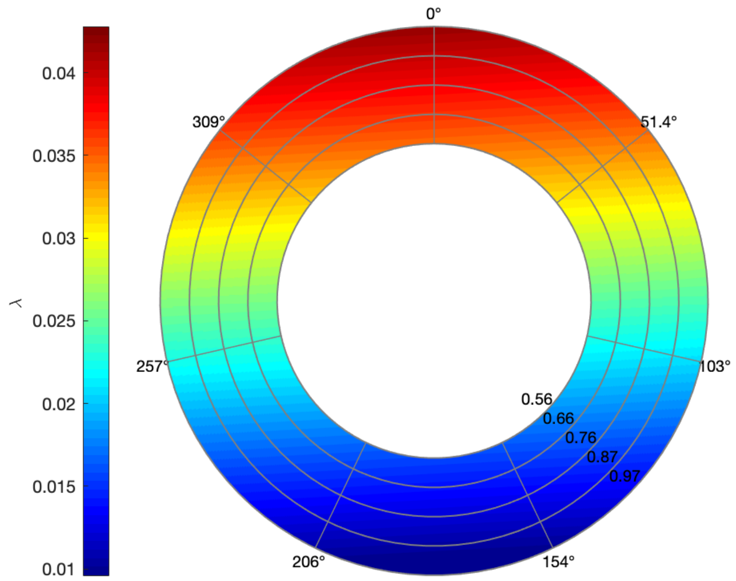

Figure 3.2: Induced velocity distribution in the rotor

The distribution reported in Figure 3.2 is as expected. The minimum value of λ is still positive, meaning that no upwash induced velocity is obtained, this lying completely within expectations.

The second paper used is from S.S. Houston and R.E. Brown [10] . In this work they study the inflow on an helicopter descending in autorotation without action of the engine. The distribution obtained by Brown and Houston can be observed in Figure 3.3.

As it can be seen, both distributions are very similar, although some differences may be observed, arising from the difference in the nature of the problems studied. However, our induction model gives the qualitative results that it should.

One should not try to reproduce the magnitude of the induced velocity in m/s, as it is a different machine (an helicopter in autorotating descent vs only a rotor) and very different results are to be expected. However, when working with dimensionless variables, magnitudes can be compared. Unfortunately, results in [10] are given with

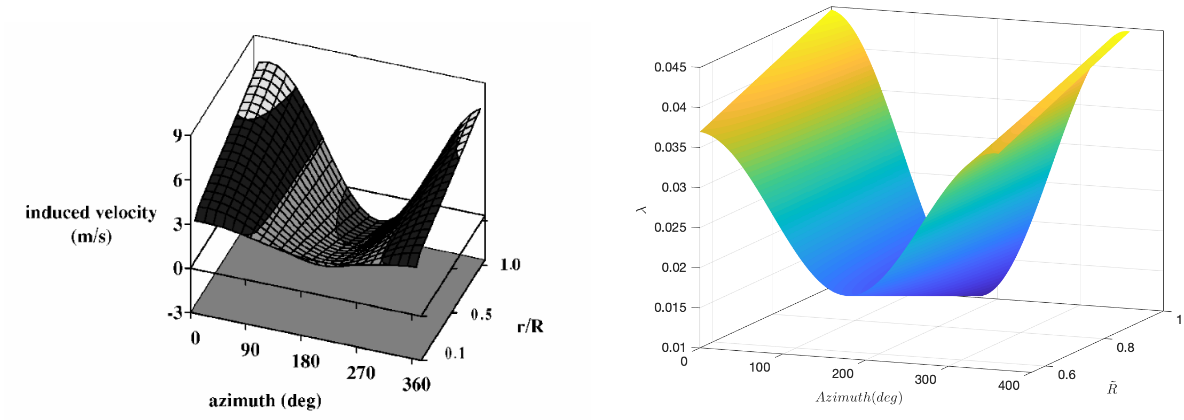

Figure 3.3: Comparison of the induced velocity distribution obtained by Houston and Brown [10] (left) and by our model (right) .

dimensions, but quantitative results can be used to compare the order of magnitude of the induced velocity obtained, which should be similar in non-dimensional terms.

The study in [10] consists in the study of a Puma helicopter descending in autorotation in an inclined plane. This helicopter is propelled by a four-bladed rotor, as our validation geometry, with a diameter of 15 m. The results in Figure 3.3 are obtained when the forward speed is at 80 knots. Brown and Houston study as well the rotorspeed at different values of the forward velocity for the autorotating descent, as shown in Figure 3.4.

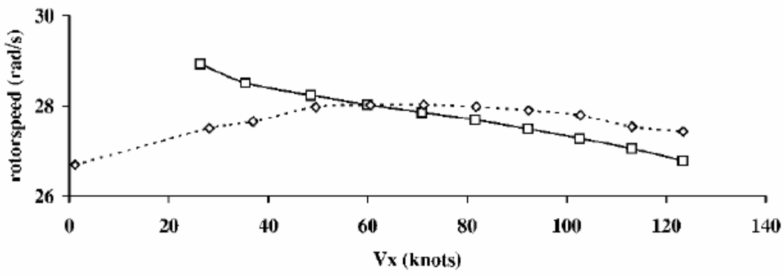

Figure 3.4: Evolution of the rotorspeed in autorotating descent for different values of forward velocity, results from [10]

Then, at 80 knots of forward speed, the equilibrium rotorspeed obtained is around 28 rad/s. With that and the radius of the rotor, the maximum non-dimensional induced velocity obtained by [10] is:

$$\lambda = \frac{V_i}{\Omega R} = \frac{9}{28 \cdot 7.5} = 0.043 \; . \tag{3.1}$$

Comparing that to the maximum induced velocity obtained in the present work, which is $\lambda = 0.045$ it can be deduced as well that the quantitative results obtained with the implemented inflow model are correct.

The results of the inflow in Figures 3.2 and 3.3 are the total induced velocity at each point in the rotor, but this inflow has the contribution of three parameters. These figures are obtained for a given time advanced in the simulation, and they are observed to be nearly constant once the equilibrium position is reached. The evolution of these parameters in time with the case run with the validation geometry is shown in Figure 3.5.

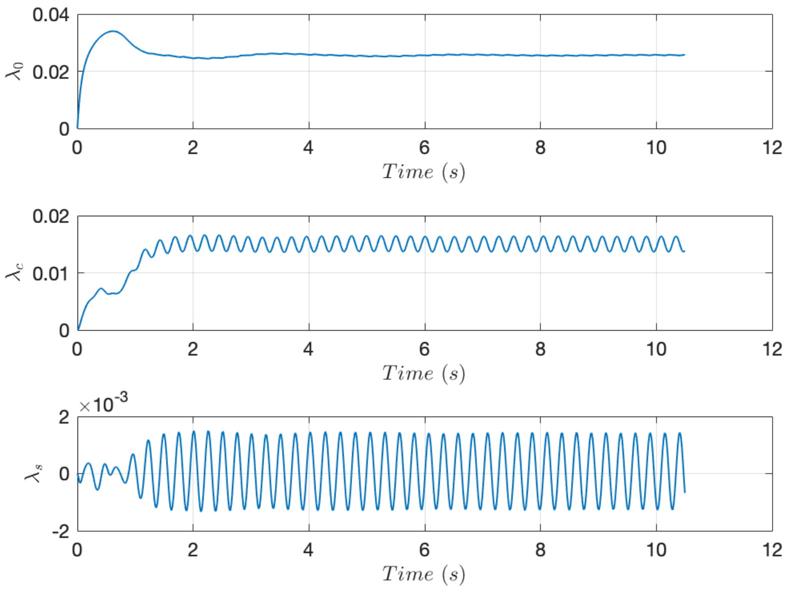

Figure 3.5: Evolution of the inflow parameters in the simulation

The behavior is the expected one: the mean inflow parameter converges to a stationary value, while the cosine and sine parameters vary periodically but are bounded, taking into account that the simulation converges to an equilibrium: the rotor stays at a given position and the rotation speed is constant. The bounded periodic variations affect much more the sine and cosine parameters since they are more influenced by the pitch and roll moments of the rotor, which oscillate due to the flapping restriction. Furthermore, as in [10], the mean inflow parameter and the sine parameters are of the same order of magnitude, while the cosine parameter is an order of magnitude smaller.

3.3 Aerodynamic model

To validate the aerodynamic module as a whole, the intention is to compare the main result of the simulation with the experimental data provided by Christof with his machine [4]. The main result is the energy output, not measured as a Power but as a Moment.

The rotation of the rotor is transmitted through the OTS to the ground station, which turns a generator. Therefore, the moment experienced at the ground station is the one that should be replicated.

In order to make this validation possible, the same parameters of Christof's machine are used in the simulator: wind speed, lengths of tether/OTS and of the anchor kite cable, dimensions and masses of the blades and rotor hub, collective pitch angle of the blades, rotation speed limit, and inclination angle of the rotor.

Christof's experiment was carried out with a variable wind, of maximum speed of 7 m/s and with an average of around 4 m/s. The data provided corresponds to an instant where the wind velocity was about 5.7 m/s, and the instantaneous moment at the ground station was:

$$M_z = 3.75 \; Nm \; . \tag{3.2}$$

The simulation is performed by choosing an initial condition near the equilibrium point (expected to be Christof's equilibrium point). This initial condition is the position of the rotor, the angular velocities and the inflow parameters. As no information is held on what the final inflow parameters will be, they are initialized at 0 and left converging to their final states. Furthermore, the wind is selected as horizontal wind, of constant speed 5.7 m/s, to match with the experimental data.

Regarding the rotation speed, the point at which Christof's data is collected, which is at the maximum allowed rotation (115 rpm), could be in one of the following cases:

- The rotation speed equilibrium point
- A rotation point with negative derivative with respect to the rotation speed, this is, a negative moment is generated with this rotation speed and so it tends to decrease with time
- A rotation point with positive derivative, this is, a positive moment is generated and so rotation speed tends to increase

The point at which the data was collected is expected to be in the last case, because otherwise no energy would be extracted, and even provided to the system. The result obtained is shown in Figure 3.6.

Take into account that the minus sign shown in Figure 3.6 is coherent with the fact that the graph shows a moment extracted from the system, hence negative. The value obtained is around

$$|M_z| = 9.85 \; Nm \; . \tag{3.3}$$

This value is shown to be higher than the one obtained by Christof in his experiment. Although it is not achieved the exact same result, the simulator obtains an energy extracted that is of the same order of magnitude and very similar. The fact that the moment obtained in the simulator is higher than the one in reality is

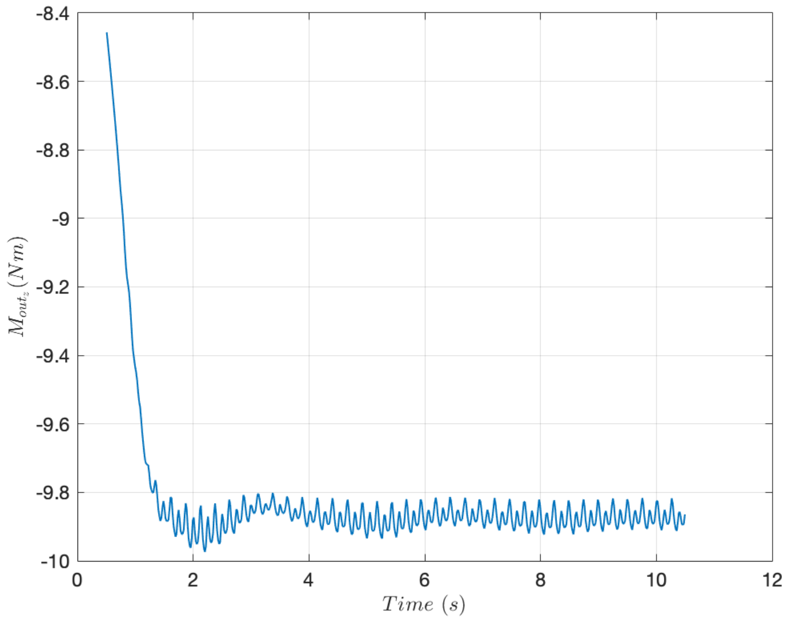

Figure 3.6: Simulated Moment extracted from the rotor and transmitted to the ground station

also a positive sign: this difference may be accounted to several losses that are not modeled.

One of this losses is the OTS inertia and drag, since it is expected to be higher than the drag of the tether, which is static at the equilibrium point, and not rotating as the OTS is. Another one is the friction in the mechanism that limits the rotation speed of the rotor.

However, another element probably affecting the result is wind. The experimental data corresponds to an instant associated to a wind speed of 5.7 m/s, but the wind showed high variability and due to the inertia of the OTS and in the rotation of the rotor, the effect arriving at the ground station would correspond to an earlier moment. Actually, if the speed in the simulator is reduced to 4 m/s, the speed averaged in the experiment, the result is much closer to the experimental one, being $|M_z| = 4.25\ Nm$.

Apart from the moment arriving at the ground station, there are data as well regarding the vertical force at the ground station. This vertical force measured is the combination of the action of the rotor and of the kite. The resultant vertical force is

$$F_z = 200\ N\ . \tag{3.4}$$

This force corresponds to the axis perpendicular to the ground station, which coincides with the $\mathbf{k_b}$ axis. The simulator results are shown in Figures 3.7a and

3.7b.

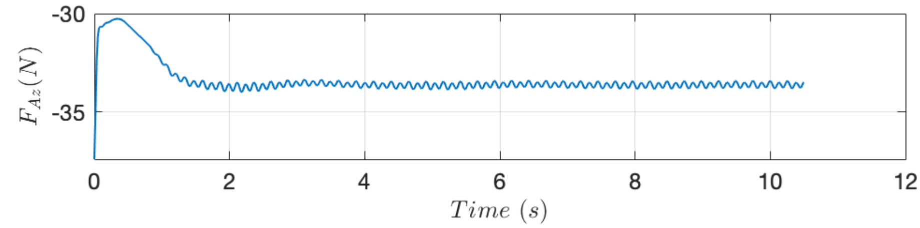

(a) Aerodynamic force of the rotor in body axis

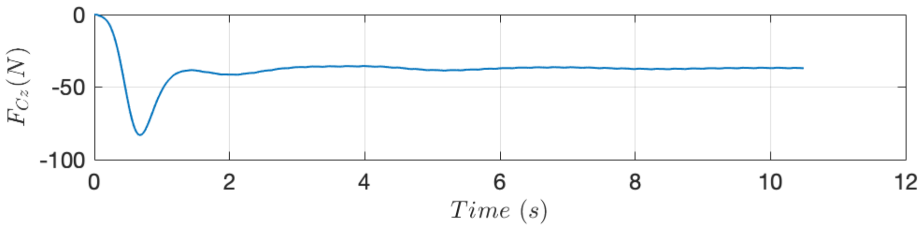

(b) Anchor kite force in body axis

Figure 3.7: Vertical ($\boldsymbol{k_b}$) forces acting on the ground station: rotor aerodynamic force and anchor kite force

A total force of $F_z = 82\ N$ is expected to arrive at the ground station according to the simulation. This force is far from the experimental result, but this should not be interpreted as a bad sign. Since the vertical force is the combination of rotor and kite, there is no way to know the expected contribution of each of them. The kite has not been modeled as it is, and it is its effect (helping the rotor stay stable in its position) what has been modeled. Therefore, the force in the kite is not expected to meet the real result and hence the total vertical force is not expected to be met. However, this result helps to understand that actually the anchor kite is generating a bigger force than the one modeled in the simulator, but that this force does not affect the behavior of the rotor apart from stabilizing it. The kite effects important to the system can be assumed to be modeled with the enough accuracy to represent the reality of the energy generation by the rotor, which is the ultimate goal of the simulator. With all this, it can be concluded that the model roughly corresponds to the system that is simulated. Further studies can be made to verify that the model has been built properly and that the aerodynamic behavior of the rotor is the expected one.

First of all, the lift generated by each blade can be checked. This force is highly dependent on the azimuth, that is, the position of the blade in the rotor plane. The blades in the advancing side should provide more lift than the blades in the retreating side. The lift distribution with time should, therefore, be periodic for a constant rotation speed. This expected behavior is then verified in Figure 3.8.

Another way to verify the model is to check the distribution of moment along a given blade, to see if there is a pattern as the one in Figure 2.3. However this study cannot be made with the parameters of this simulation. The reason is that the rotation speed at the equilibrium point is such that the aerodynamic moment generated is very high, trying to accelerate the rotation. The effect in the moment

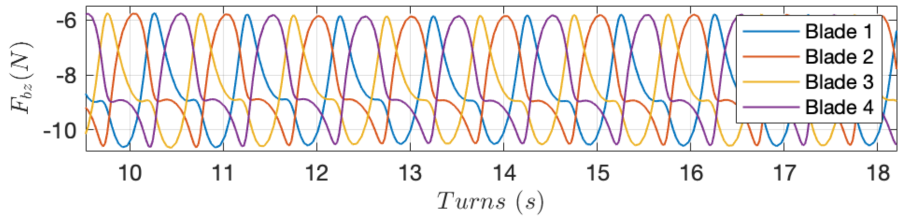

Figure 3.8: Aerodynamic lift of the blades, along $\mathbf{k_b}$ axis

distribution along the blade is that the autorotation point is moved out of the blade, so that the whole blade is generating a positive moment, although the trend of the positive moment is obtained.

Therefore, to better see this distribution another simulation has been performed in which the rotor has been let to reach one of its equilibrium points, generating a very small aerodynamic moment. The distribution of the moment contribution of one of its blades is shown in Figure 3.9.

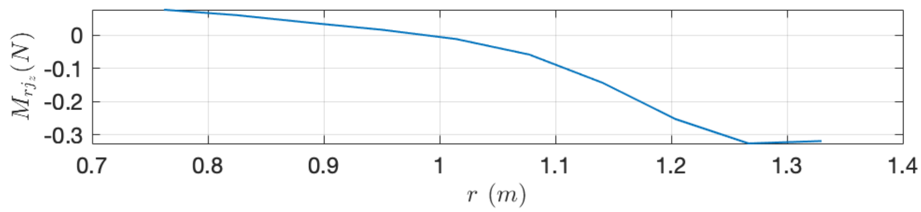

Figure 3.9: Contribution to the moment of the different sections of a given blade, in $\mathbf{k_b}$ axis

The distribution of Figure 3.9 shows a blade with negative net moment, although very small, hence contributing to decelerate the rotation. In this distribution, a very similar pattern to the one in Figure 2.3 is obtained. It should be taken into account the big gap between the center of rotation and the beginning of the blades of the geometry of the current situation. For that reason, the distribution of Figure 3.9 is of the form of the one in Figure 2.3, although the first part of the blade is cut out (the cut is at the right of the maximum positive moment obtained). Hence, the distribution of moments along the blades is as well verified to be the one expected.

Chapter 4

Numerical results and parametric analyses

Contents

In this chapter the results of the study with the dynamic simulator will be reported. The objective is to shed some light on several parameters that are inputs to the system in order to acknowledge their influence and their effect on the behavior of the rotorcraft.

4.1 Main simulation results

The "main simulation" is referred to as the simulation done in order to perform the verification and validation process. Therefore, the geometry and parameters used are the ones that match the characteristics of the experiment carried out by Christof. The wind is static and at a speed of $V_w = 5.7\ m/s$. The results of the induced velocity have already been shown and commented upon in section 3.2. First of all, the evolution of the position of the rotorcraft is analyzed.

Figure 4.1 shows the evolution of the three components of the position with time. Figure 4.2 is a representation of the path followed by the rotorcraft in its lateral projections. The green point shows the initial position while the red point corresponds to the final one. The initial position selected to start the simulation is actually very near to the final position, so taking into account that this initial

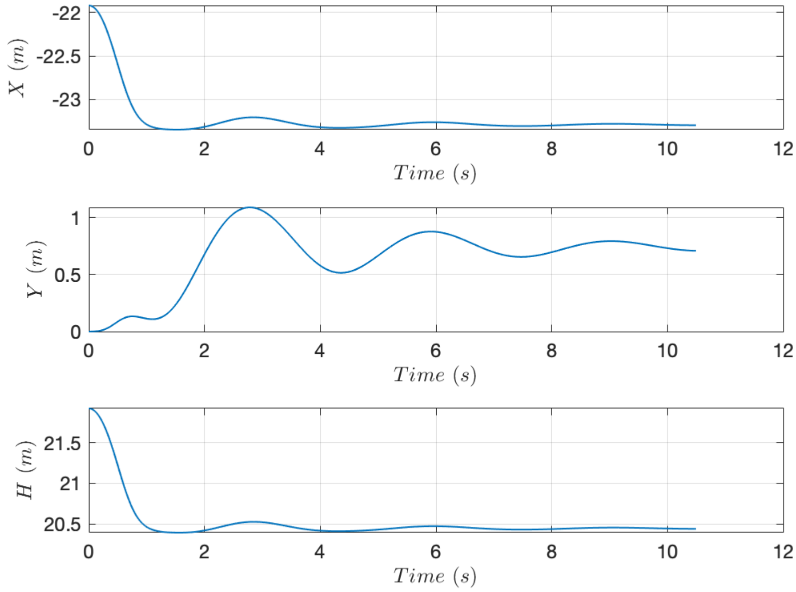

Figure 4.1: Position of the rotorcraft

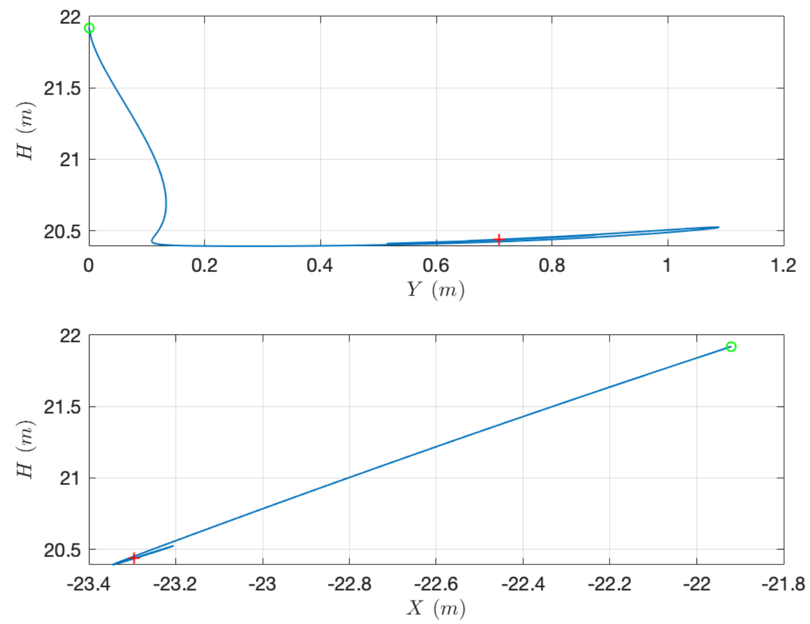

Figure 4.2: Lateral projection of the rotorcraft's path

position is chosen as approximately the equilibrium position shown by Christof's machine, this falls totally within the expected result. However, although in Figure 4.2 it may seem that the rotorcraft ends in a stationary position, Figure 4.1 shows that it seems to be slightly oscillating around that position. This, again, falls within the expectations, as no flapping and lagging movements are allowed in this rigid rotor, and elasticity of the materials is not taken into account.

It may be noticeable as well that the rotorcraft ends at a position with X and Y coordinates different from the initial ones, even if the anchor kite is modeled as a spring with a damper that pulls the rotorcraft towards the initial position. Regarding the X coordinate this effect is normal since the rotorocraft traction force is in the H-X plane, so the spring force and tension force on the tether end up at an equilibrium with the traction force and, hence, the X and H coordinates are expected to change. However, the Y coordinate oscillates around a position just 0.8 m in the positive direction of Y axis but at an equilibrium point it may be expected that there exists no displacement in the Y direction, mainly because of the spring-damper action.

In order to achieve this equilibrium position there must exist an equilibrium of forces between the aerodynamic lateral force and the anchor kite lateral force.

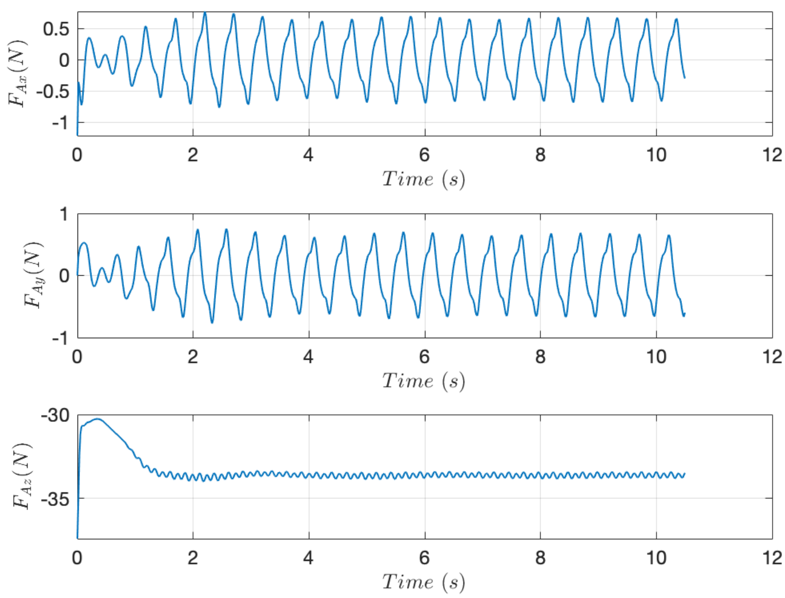

Figure 4.3: Aerodynamic forces of the rotor, body frame

Figure 4.3 shows the aerodynamic forces of the rotor in the three components of the body frame. In the Y coordinate one can observe an oscillatory behavior around 0, but this is the body frame, which is rotating, so this does not show the Y-component force that is expected. Nevertheless, seeing the forces in the body frame helps to analyze the main force exerted by the rotor, which is the lift, much higher in magnitude than the other components.

In Figure 4.4 the aerodynamic forces of the rotor are shown in the Earth frame. All components of the force show a periodic behavior, due to the intrinsic periodic nature of the rotation movement. The period of the oscillations is of one quarter of a revolution, as the rotor in this study has four blades. This figure shows the expected result: the rotor is generating a force towards the positive Y-axis. This behavior is

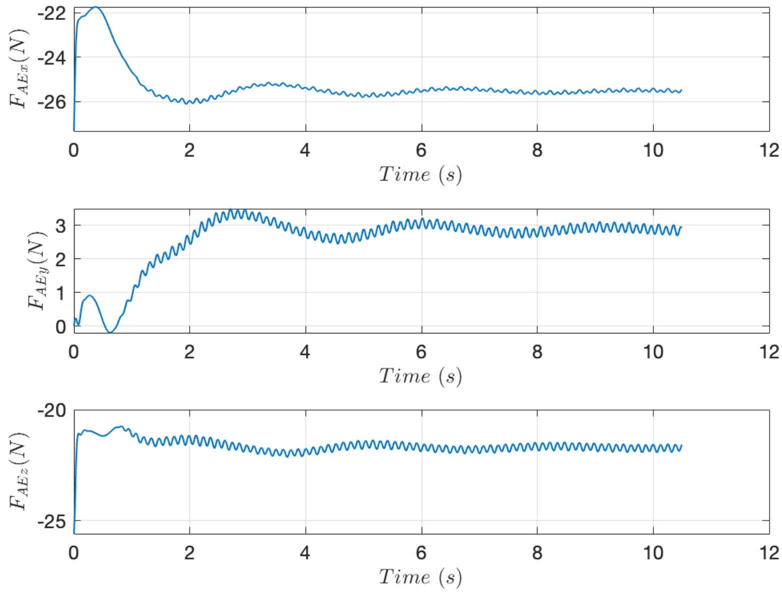

Figure 4.4: Aerodynamic forces of the rotor, Earth frame

actually not wrong. Juan de la Cierva experienced this effect in his first autogyros. His C.3 autogyro showed "a tendency to fall over sideways". He realized as well that one of his models was flying properly, and that this model had the blades made of flexible palm wood. The fact that the flexible rotor blades were responsible for the success of the flight is what moved de la Cierva to create articulated rotor blades on the autogyro and he started to use flapping blades in his designs. The flap hinge was able to eliminate the rolling moment on the aircraft in forward flight due to the asymmetry of the flow over the rotor [33].

In fact, the asymmetry of flight is a property characteristic of rotors, both in autogyros and helicopters. To better illustrate it, Figure 4.5 shows how the lift asymmetry problem in a rotor is generated. Note that this figure has been extracted from [7], so the convention is not the one used to derive the model of the present work.

In hover flight (Figure 4.5a) all azimuth positions have the same velocity distribution, given only by the rotation speed and the radius. However, in forward flight there is another component that must be added. Therefore, in the advancing side, the velocity felt by the rotor is higher than in the hover case, while in the retreating side is lower. In the retreating side a given region experiences a speed due to the rotation lower than the corresponding component of the forward speed, so that the aerodynamic velocity for the airfoils in this region is negative and, hence, this region has reverse flow. Wheatley defines in [36] the reverse flow region as the one going from 0 to $-\mu R \sin\psi$, where μ is defined as in Equation 2.35. This expression comes easily from the analytic expression for the in-plane velocity term as done by Wheatley [36].

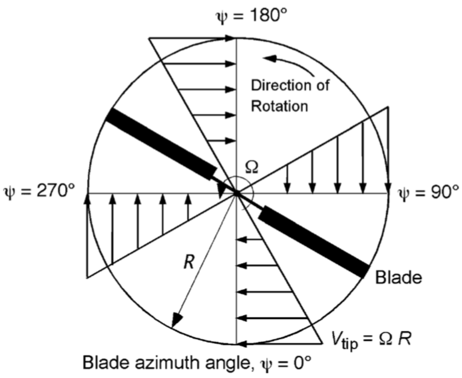

(a) Velocity distribution in a rotor in hover.

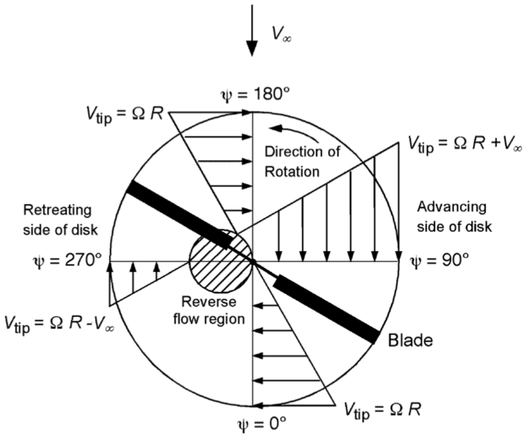

(b) Velocity distribution in a rotor in forward flight.

Figure 4.5: Difference in velocity distribution on a rotor in hover and forward flight. Source [7]

Going back to the analysis of the results, the lateral force is counteracted by a lateral force coming from the anchor kite, as it can be observed in Figure 4.6.

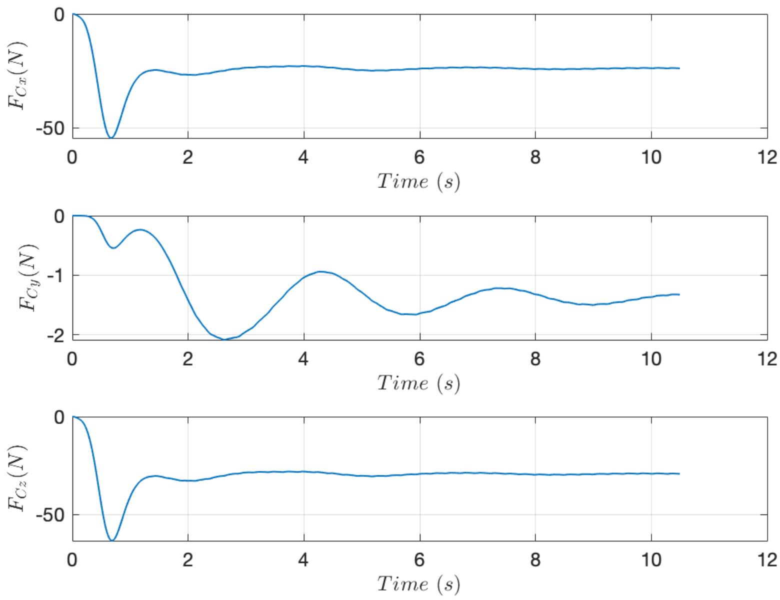

Figure 4.6: Aerodynamic forces of the anchor kite, Earth frame

The anchor kite is, as expected, generating a force in the negative Y-axis to counteract the resultant effect of the lift asymmetry. Furthermore, it shows, as well as the position of the rotor, an oscillatory behavior of the forces, of small magnitude, due to the rigidity of the rotor. While in Figure 4.6 a similar magnitude is observed for the X and Z components of the force, this force is actually in the body Z axis (see Figure 3.7b), as the rotor inclination is around 45º.

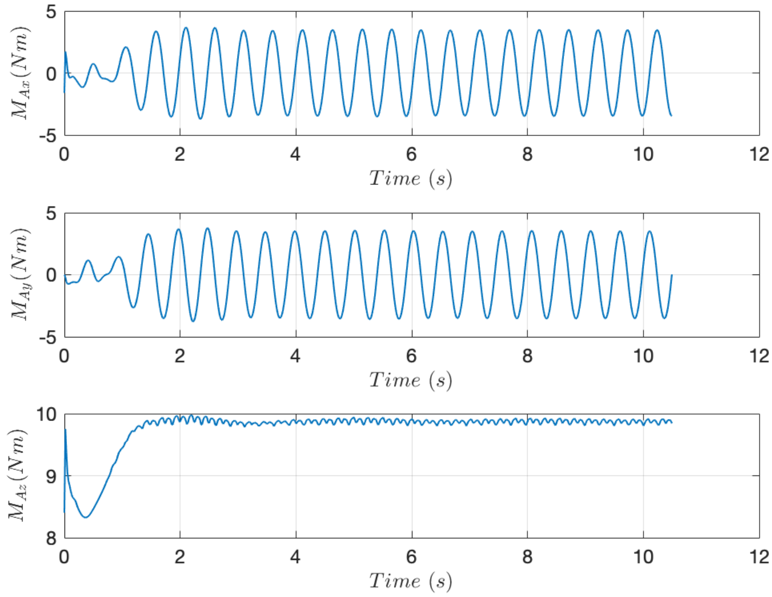

Figure 4.7: Aerodynamic moments of the rotor, body frame

Passing to the aerodynamic moments of the rotor, in Figure 4.7, a behavior very similar to the aerodynamic forces is found. A main component is observed in the Z body-frame axis, corresponding to the autorotation moment, while in the X and Y axis it oscillates around 0. In this case, if the moments were expressed in the body frame, it would be found a net positive upsetting moment around X-axis, because of the asymmetry of lift. The autorotation moment (component Z in Figure 4.7) is very similar to the extracted moment obtained in Figure 3.6, since the OTS inertia and drag are not accounted for, and it is expected to be much higher than that of a simple tether.

Recovering the result shown in Figure 3.6, the moment extracted from the rotor to move the ground station is:

$$|M_z| = 9.85 \ Nm \ . \tag{4.1}$$

And, being the ground station rotating at 1.92 rps, the energy that is extracted from the machine, without accounting for all the losses is:

$$P = 118 \ W \ . \tag{4.2}$$

Moving on, although the blade forces and moments have already been assessed in Chapter 3, a final analysis regarding the blades can be made, and it is the study of the angle of attack obtained along the blades. Figure 4.8 shows this result. As it could be expected after all the explanations given in Chapter 2, the angle of attack shows a decay from root to tip, being the maximum angle of attack obtained of 27º

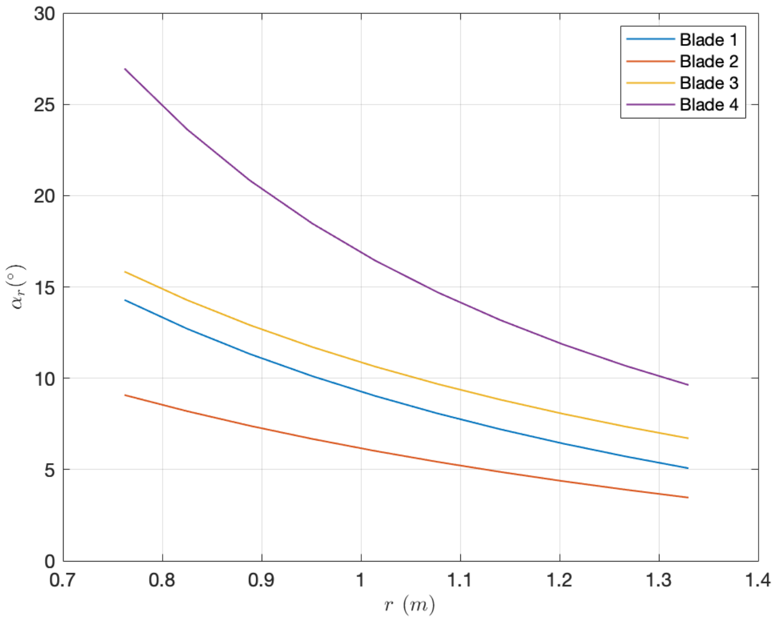

Figure 4.8: Angle of attack along the blades

and the minimum of 4º (not in the same blade). There is no point with negative angle of attack, since the rotor is inclined at around 45º and hence, the wind hits the rotor from below. As the tangential velocity due to the rotation speed increases towards the tip, and being the vertical component (vertical to the rotor plane) of the velocity (this component comes from the aerodynamic velocity) constant along the same blade, the angle of attack diminishes. Even if the rotor is inclined, if it is going upwards it could arrive a moment in which the velocity of the center of mass of the rotor is higher than the wind speed, hence making negative the aerodynamic velocity component perpendicular to the rotor, but that is not the case in this simulation.

In Figure 4.9, the velocity of the rotor in the Earth frame is represented. After an initial time where all the variables that were "guessed" for initial conditions of the simulation converge to their normal values, the rotor achieves equilibrium, where the velocity of the rotor oscillates very slightly around zero.

Finally, the angular velocity of the rotor is shown in Figure 4.10. The angular velocity is represented in the body frame, therefore the Z component corresponds to the rotation speed of the rotor. In this component's plot, it is represented the evolution of the rotation speed together with the target maximum speed. The final equilibrium speed is very near to the target one, $\omega = 115\ rpm$, and the small gap observed corresponds to the fact that the implemented PID has only a proportional action, although it gets very near to the objective. In the other two components, a very small angular velocity appears, with periodic behavior.

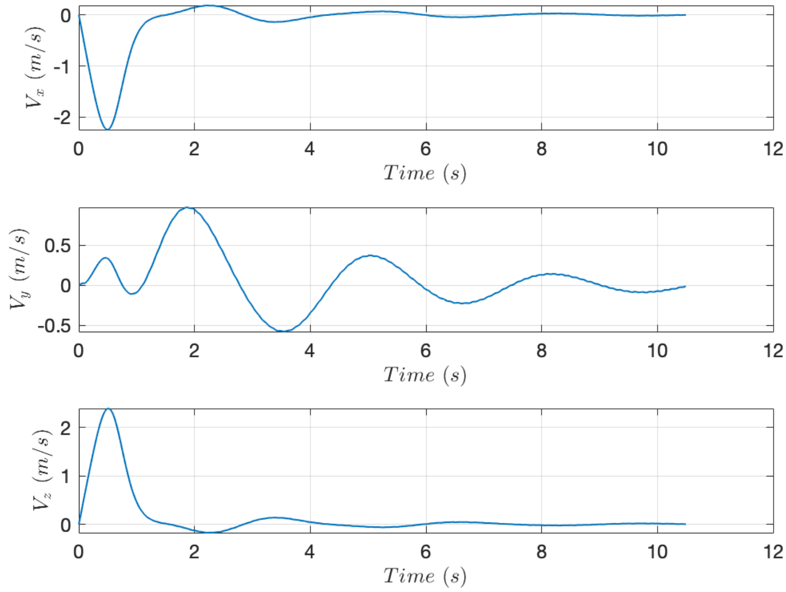

Figure 4.9: Rotor velocity evolution. Earth frame

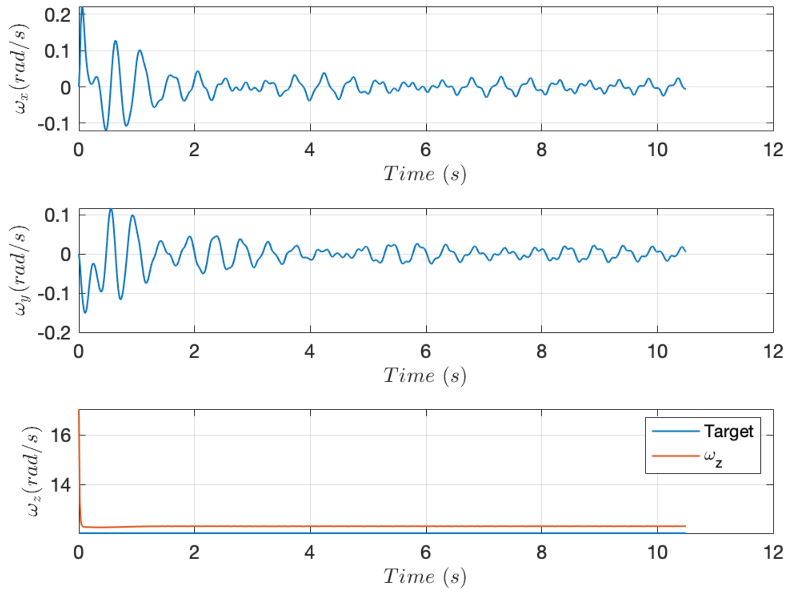

Figure 4.10: Rotor angular speed evolution. Body frame

4.2 Predicted equilibrium points

In the simulation performed in order to validate and verify the model, with the above mentioned results, the angular speed has not been let to achieve an equilibrium. The objective of this section is, therefore, try to make an easy estimation of what would be the equilibrium points of the angular speed.

In order to do so, the aerodynamic module is isolated from the rest. The induction model is also neglected to simplify this study, so it should be taken into account that the rotation speeds obtained as equilibrium points are expected to be a little bit different in reality, since the induction speed may affect the derivatives and the behavior slightly.

The way to obtain simply these equilibrium points is to calculate the autorotation moment generated for several values of the rotation speed. The wind speed is set to be 5.7 m/s and no collective pitch angle θ is used. The inclination of the rotor is set at 45º.

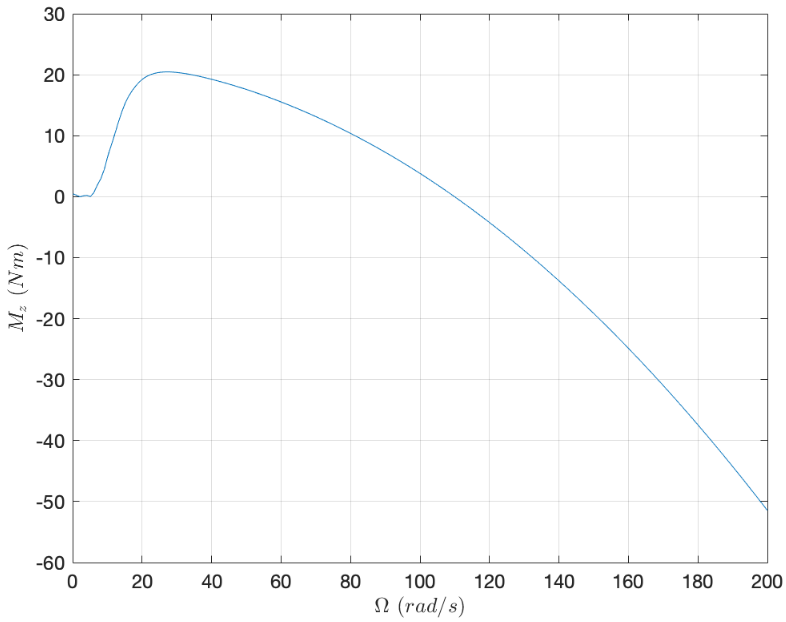

Figure 4.11: Predicted equilibrium points for $\theta = 0º$

Figure 4.11 shows the autorotation moment generated for several values of the rotation speed. Equilibrium points are such that generate no net autorotation moment. One clear equilibrium point is obtained at high rotation speed, at $\omega = 110\ rad/s = 1050\ rpm$. This equilibrium point is stable: if the rotor is at a rotation speed at the left of this equilibrium, the positive autorotation moment accelerates the rotation speed to the equilibrium point. If the rotation speed is at the right of the equilibrium point, the autorotation moment is negative and decelerates the rotation to the equilibrium point.

But, apart from this equilibrium point, a close up look to the low speed region is obtained in Figure 4.12. It shows two more equilibrium points. The one at the left is stable, while the second, at the right, is unstable since at both sides of the equilibrium the moment is such that tends to make the system go away from the equilibrium point. For the left equilibrium point, although being stable, it wouldn't show a stable behavior for the real machine, as the span of rotational speeds at the

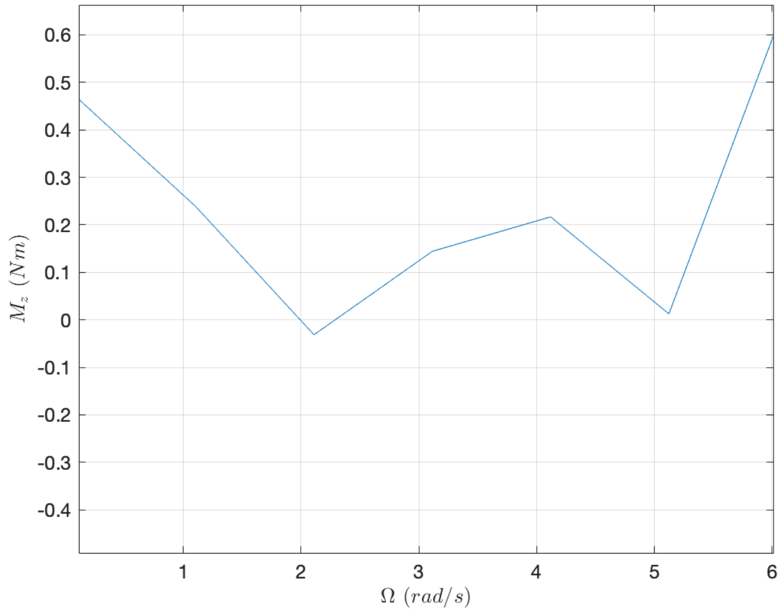

Figure 4.12: Close up look at the low speeds of the predicted equilibrium points for $\theta = 0^{\text{o}}$

right of the equilibrium that give negative moments is very small. Therefore, an overshoot when arriving at equilibrium or any perturbation would easily break the equilibrium.

D. Rezgui, in his work [44], realized as well that autorotation is a phenomenon that has multiple equilibrium points, rising the concern that a given maneouvre may cause the autogyro of his study to jump from the stable equilibrium point to an unstable equilibirium point.

The result of Figure 4.12 would mean that if no PID was used to limit the maximum rotation speed, the rotor would tend, for a $\theta = 0^{\text{o}}$, to accelerate towards a very high rotation speed. This somehow justifies the need to limit the rotational speed with this design, since its natural behavior is to converge to very high rotational speeds that the structure would not be able to bear.

To see the effect of the collective pitch angle on the predicted equilibrium points, the same study has been applied for several pitch angles, spanning from $\theta = -2^{\text{o}}$ to $\theta = 6^{\text{o}}$. The results are shown in Figure 4.13.

The change in the curves is clearly perceptible. As a general trend. the shape of the curve is very similar for all pitch angles. There always exists a stable equilibrium point at high speeds, being this equilibrium point higher as the pitch angle increases. Together with the rotation speed at the equilibrium point, the maximum values of autorotation moment also increase.

An interesting behavior is shown for the low rotational speeds. Figure 4.14 shows a close up look at the low rotational speed behavior. Contrary to what happens at

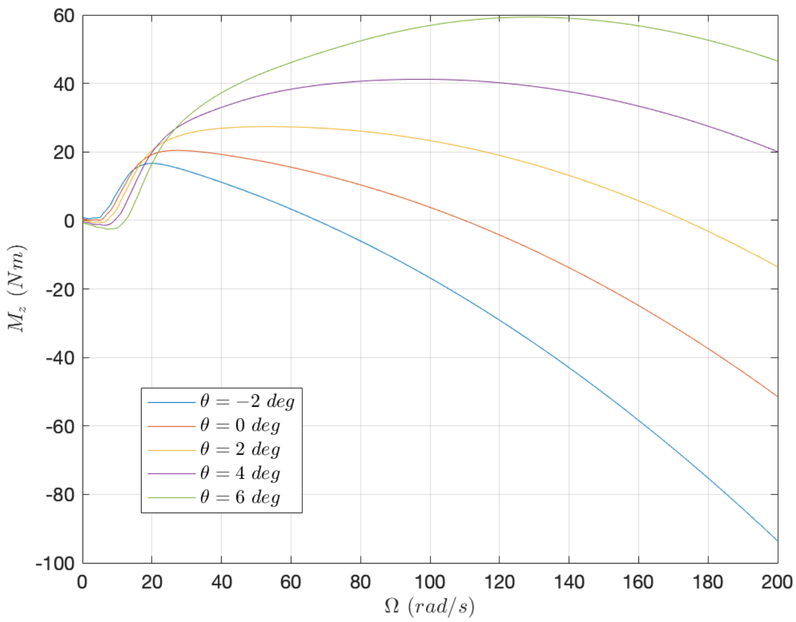

Figure 4.13: Predicted equilibrium points for several values of θ

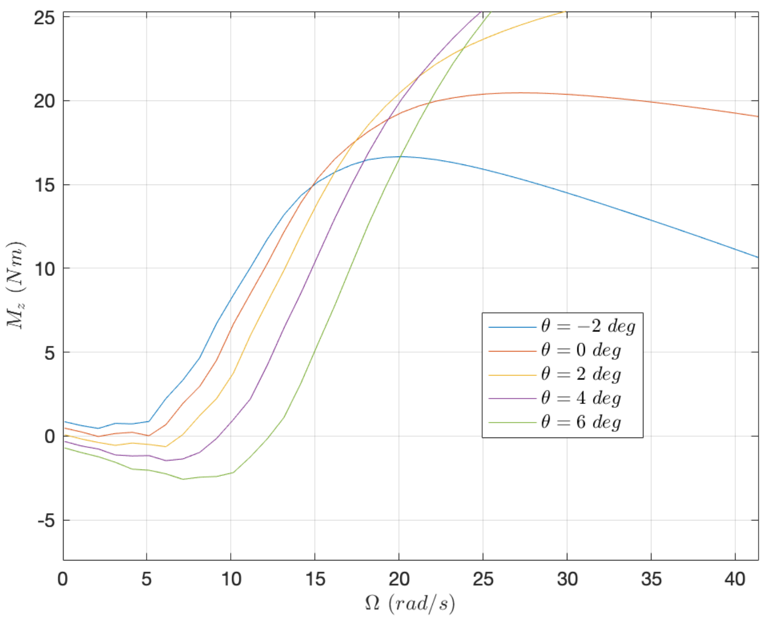

Figure 4.14: Close up look at the low speeds of the predicted equilibrium points for several values of θ

high rotational speeds, here the higher the pitch angle, the lower the autorotation moment, even being negative for positive values of pitch angle. This means that for low rotational speeds autorotation cannot be maintained at this value of wind speed. If the pitch angle is set to $\theta = 4^{\text{o}}$ and, if the rotor is rotating at, for example,

$\omega = 7\ rad/s$, the rotation speed will slow down to zero and autorotation will not be possible.

Therefore if, for structural reasons, the rotational speed has to be maintained fairly low (below $\omega = 15\ rad/s$) then increasing the pitch angle would produce no benefits, since the benefits of increasing pitch angle are obtained at high rotational speeds and it would not be possible to take advantage of them. In fact, up to $\omega = 14\ rad/s$, a negative pitch angle produces a higher autorotation moment than the null and positive pitch angles. Furthermore, this behavior highlights the advantage that would be obtained when it is possible to control the pitch angle, adapting it to the flight conditions.

Table 4.1 compiles the main behavior observed for changes in the pitch angle within the range of pitch angles studied.

	Low rpm	**High rpm**
θ **increase**	M_z decreases	M_z increases
θ **increases**	M_z increases	M_z decreases

Table 4.1: Resulting behavior in the equilibrium points for changes in pitch angle θ

4.3 Effect of the number of blades

The number of blades of the rotor is one of the most important parameters in the design of a rotor. Increasing the number of blades gives the rotor a higher solidity, but adds mass that can result in a disadvantage. There exist commercial helicopters from 2 blades to 6 blades, depending mainly on the purpose of the helicopter. Helicopters with 2 blades are typically those that carry only the pilot or a maximum of 2 people, for recreative use. The vast majority of helicopters use 3 or 4 blades, and some special designs use 5 and 6 blades.

Regarding autogyros, nowadays they use only 2 blades, since they are very light weight machines carrying one or two people and typically used for recreative flight. The few models and prototypes of RAWES are mainly of 3 and 4 blades.

Therefore, a parametric study has been performed changing the number of blades used in the model, with the corresponding update in the mass of the rotor. However, the same parameters of the simulation are maintained for all cases: same dimensions of the blades, inclination of the rotorcraft, maximum rotational speed, pitch angle and wind speed.

Figure 4.15 shows the result on the most important magnitude of the simulation: the extracted moment. The main conclusion extracted from the figure is that the design that extracts the highest moment and, hence, the highest power from the system is the 5 blades model. It seems as well that the increase from 3 to 4 blades is much higher than from 4 to 5 blades. The average no-losses power extracted from

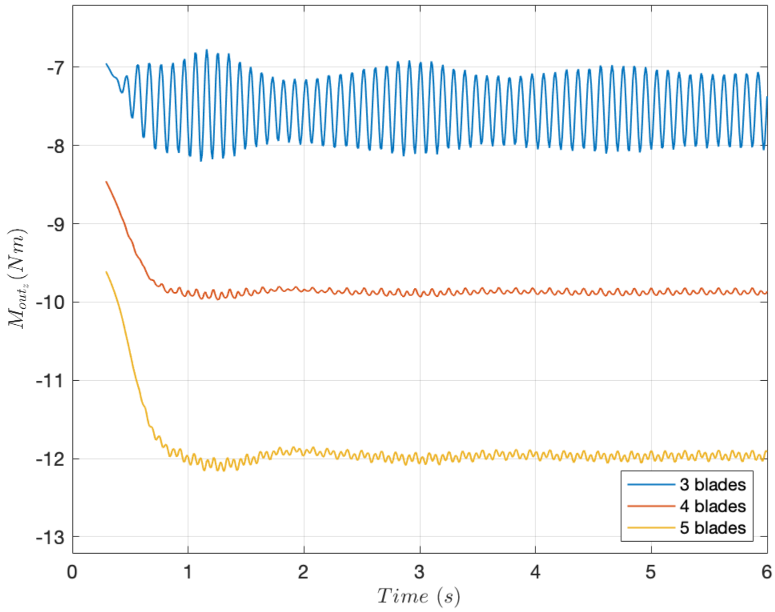

Figure 4.15: Extracted moment for different numbers of blades

each design would be:

$$P_3 = 90\ W \qquad P_4 = 118\ W \qquad P_5 = 144\ W\ . \tag{4.3}$$

It seems that adding a blade is not a drawback, which is normal regarding the low weight of the blades of the prototype whose characteristics have been modeled in the simulator. Therefore, the best design in the conditions studied should be either the 4 or the 5 blades one, since the marginal benefit passing from 3 to 4 blades (+31%) is worth it. Between the 4 and 5 blades designs the marginal difference in power is of +22%, less than the difference from 3 to 4 blades, but still a benefit in power output. Besides the power output by itself, some other characteristics have to be taken into account. In this simulation the addition of blades has been fairly simple: the blades are positioned at the same angle from one another and only the weight corresponding to the blade is added. In a real prototype, adding a blade would not be that simple: it means adding complexity to the structure, which may add some weight apart from the weight of the blade itself, a new hinge mechanism (if flapping, as would be expected, is allowed) that would add on weight, new actuators to change the pitch angle (if this type of active control is implemented), and other side drawbacks as well, as it is the case of higher energy required for the take-off and problems regarding repair and maintenance. Furthermore, changing the number of blades makes the machine completely different, so a new process of design optimization should be performed in order to be a be to compare the designs: choosing the optimum radius, chord, airfoil profile and also the flight parameters would be optimized. Therefore, this analysis helps compare the effect of changing the number of blades when all parameters are kept constant. If the parameters of the machine to be used were the ones in this study, then the 5 blades design would be the best one. However, for all differences made in the design or in the model (addition of control, removal of the kite, larger scale, different materials) this question should be assessed again.

Another result arising from Figure 4.15 is the oscillatory behavior. The difference in the amplitude of the oscillations that the 4 and 5 blades designs produce with respect to the 3 blades design is very well known. This last case shows an amplitude of 13% around the average value, which is clearly a lot, compared to the 1% of the 4 blades design and the 1.5% of the 5 blades design. These high oscillations in the 3 blades design would make it much more difficult for the control of the rotor, making it more unstable and submitting the structure to more fatigue, so they are not desired. However, this behavior is observed for unaltered values of radius of the rotor, chord and every other parameter with respect to the base case. The design could be improved and the oscillations be reduced, but it is a good estimation of the trend.

If the anchor kite was aimed to be removed and substituted by active control in pitch and by including flapping hinges or flexible materials, then another key parameter to take into account in the design would be lift. The lift force would be the one in charge of maintaining the rotor on air.

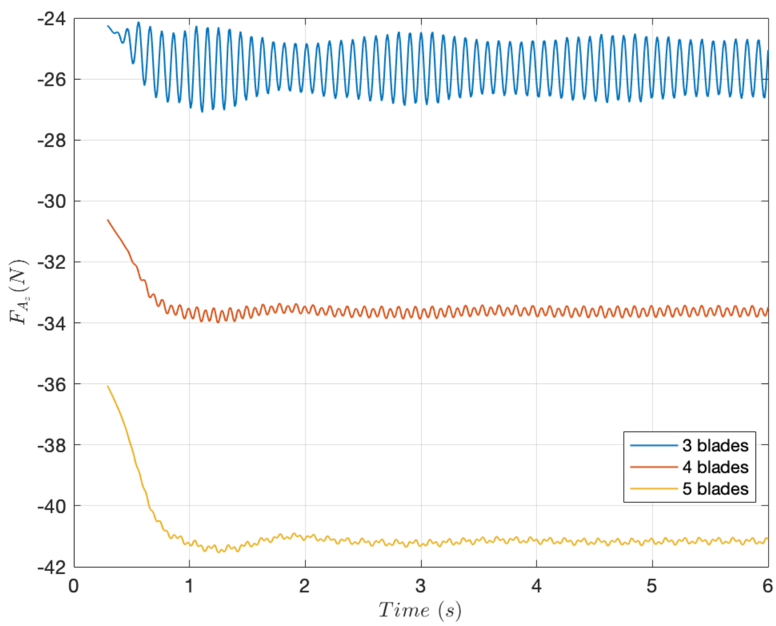

Figure 4.16: Lift generated by the rotor for different numbers of blades. Body frame

Figure 4.16 represents the lift generated by the three designs in the body frame. It is observed a behavior similar to the one regarding the moment generated. There is an increase in lift with the increase in the number of blades. Again the 3 blades design shows very high amplitude of the oscillations while the 4 and 5 blades design show low amplitude oscillations, slightly lower for the 5 blades design in this case. The lift force is needed to sustain the weight on the rotor, so it is more interesting to see the load factor of each design:

$$N = \frac{F_{A_z}}{W} \ , \tag{4.4}$$

and the result for the three designs are:

$$N_3 = 3.1 \qquad N_4 = 3.6 \qquad N_5 = 3.7 \ . \tag{4.5}$$

This shows again the great benefit obtained when going from 3 to 4 blades, while in the case from 4 to 5 blades the increase is much lower. Anyway, it would still be advisable to choose the 5 blades design if the design of the whole system is to be maintained as it is. However, the addition of blades also increases the the magnitude of the lateral force arising from the lift asymmetry since there is no flapping, as it can be observed in Figure 4.17.

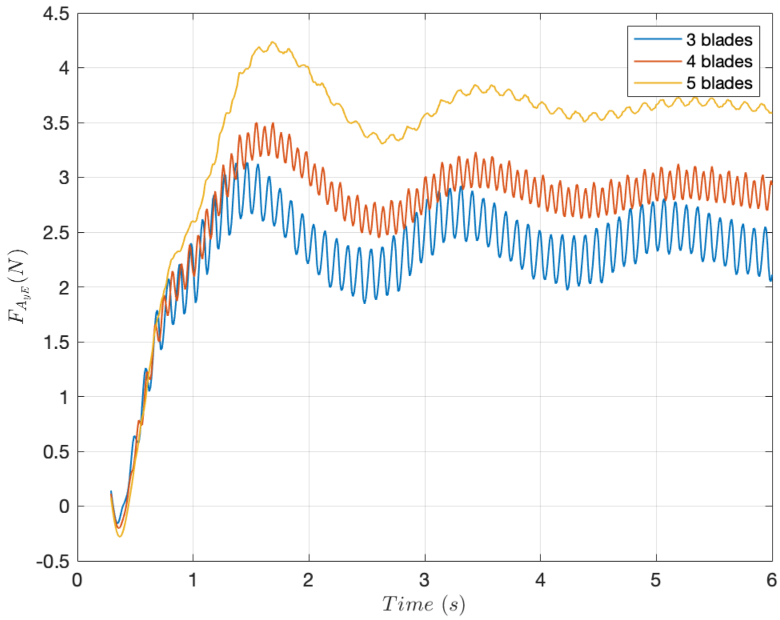

Figure 4.17: Lateral force generated by the rotor for different numbers of blades. Earth frame

Figure 4.17 represents the Y-component aerodynamic force in the Earth frame for the three designs. Now there is a clearly higher increase in this force from 4 to 5 blades is clearly higher than from 3 to 4 blades. This suggests that it may be possible that, in case of adding active control to the system, it could be advisable to stay with the 4 blades design, since more aggressive control would be required to combat the sideward force, and this control energy would be taken from the total power output, so the whole analysis should be performed to find the optimum design.

Table 4.2 sums up the results obtained for the three different designs: 3, 4 and 5-bladed rotors.

	3 blades	4 blades	5 blades
Extracted moment (Nm)	7.5	9.85	12
Power (W)	90	118	144
Lift in k_b (N)	26	33.8	41
Lateral force in j_E (N)	2.5	3	3.75
Lift to weight ratio N [-]	3.1	3.6	3.7

Table 4.2: Results for the parametric study on the number of blades

4.4 Effect of the induction model

The induction model is a necessary part of the model, that brings it closer to reality. The induced velocity in autorotation, as stated in chapter 3, goes downwards the rotor, while the flow goes upwards. The net effect is that it slows down the flow through the rotor, so the inflow model effect should be of lowering both the power output and lift force generated by the RAWES.

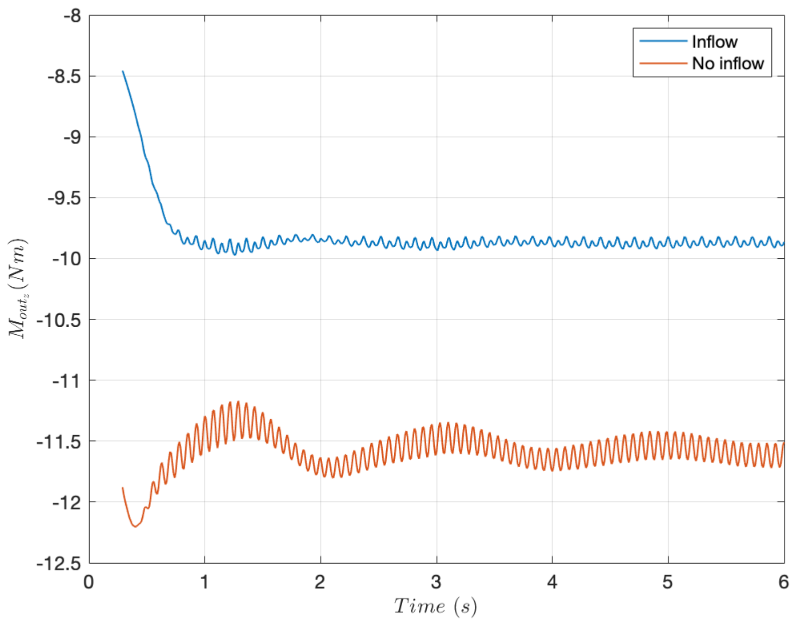

Figure 4.18: Moment extracted comparison of the model with and without inflow

First of all, the moment extracted is analyzed and represented in Figure 4.18. The expected result is obtained. The inflow generated by the rotation slows down the flow when passing through the rotor and, therefore, the available energy at the rotor is less. When converting to power units, the expected no-losses average power outputs are:

$$P_{inflow} = 118\ W \qquad\qquad P_{noinflow} = 140\ W\ . \tag{4.6}$$

An excess of 18% in the power output is obtained if no inflow model is employed, hence justifying the high importance of accounting for this effect if the objective of the simulator is to be used to properly estimate the potential energy that can be extracted from a RAWES design.

Another interesting effect can be analyzed. The inflow model actually reduces the amplitude of the oscillations. It somehow damps the effects of the forces acting on the rotor. This damps, in consequence, the oscillations generated.

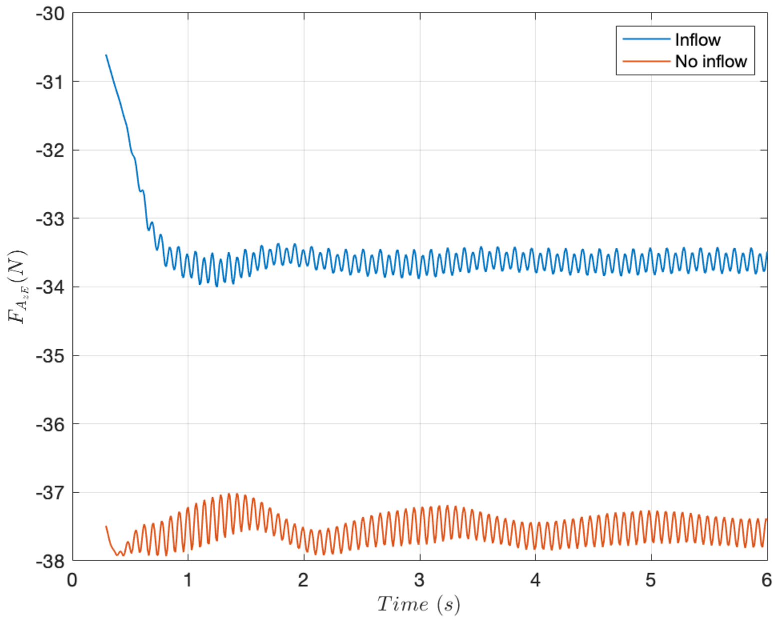

Figure 4.19: Lift of the rotor comparison of the model with and without inflow. Body frame

Then Figure 4.19 shows the lift generated by the rotor in the body frame. The lift also changes according to the expectations: the inflow effect is to lower the lift generated by the rotor and to reduce again the oscillations shown in the lift. If the inflow model was not used, the results obtained would correspond to a much higher wind speed and both the power output and the lift capabilities of the system would be highly overestimated.

4.5 Effect of the maximum rotation speed attainable

The next study is to analyze the effect on the power output of the selected maximum rotation speed. As explained in Section 4.2, the net autorotation moment of the rotor, having all other parameters unaltered, changes with the rotation speed, and not in a linear manner. That is why an analysis like the one carried out here is very interesting. If it is seen a great benefit in terms of power extraction, then it will be clear the necessity of designing and building stiffer prototypes and machines.

Three cases have been taken into account. The nominal case, a rotation speed of $\Omega = 115\ rpm$ and two more cases, one in the lower side, $\Omega = 80\ rpm$ and one in the upper side, $\Omega = 150\ rpm$. For the lift force, it would be expected an increase with the increase in the rotation speed. However, increasing the rotation speed will also make the angles of attack of the blades get closer to 0, so this expected increase in lift should not be linear.

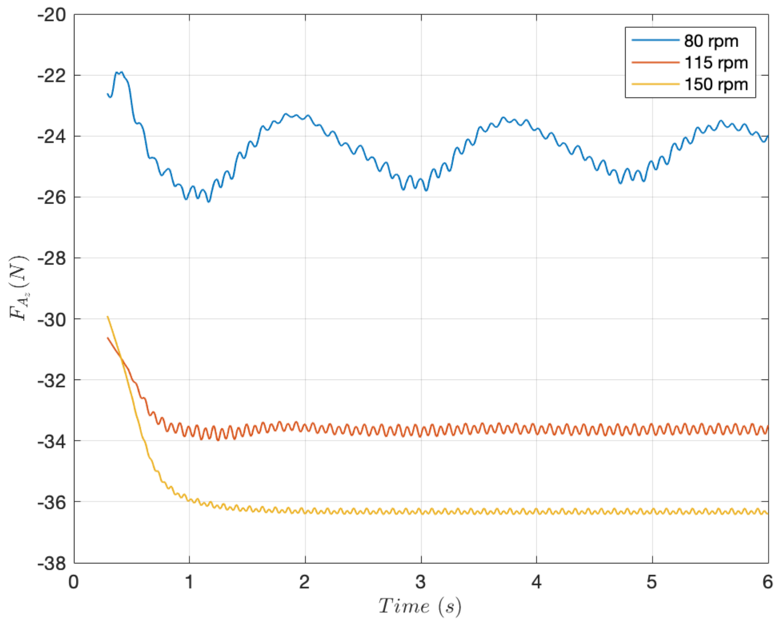

Figure 4.20: Lift of the rotor comparison for three values of rotation speed. Body frame

Figure 4.20 shows the lift generated by the rotor in the body frame, for the three different cases. The trend above mentioned is clearly observed, with a noticeable increase in lift when increasing the rotation speed from 80 rpm to 115 rpm and a much lower increase for the successive increase in rotation speed. It is noticeable as well the lower amplitude of the oscillations that are produced when increasing the rotation speed, which is expected since it reduces the relative relevance of the incoming flow that results in lift asymmetry. But it is very interesting the behavior of the lowest rotational speed. At this lower speeds another oscillation of very low frequency is clearly visible, together with the high frequency oscillation.

The extracted moment is represented in Figure 4.21 for the same three cases. In this case, a different behavior than with the lift is obtained. The lowest rotation speed provides the lowest extracted moment, and the maximum extracted moment is found for the case with $\Omega = 115\ rpm$, with a noticeable difference with respect to

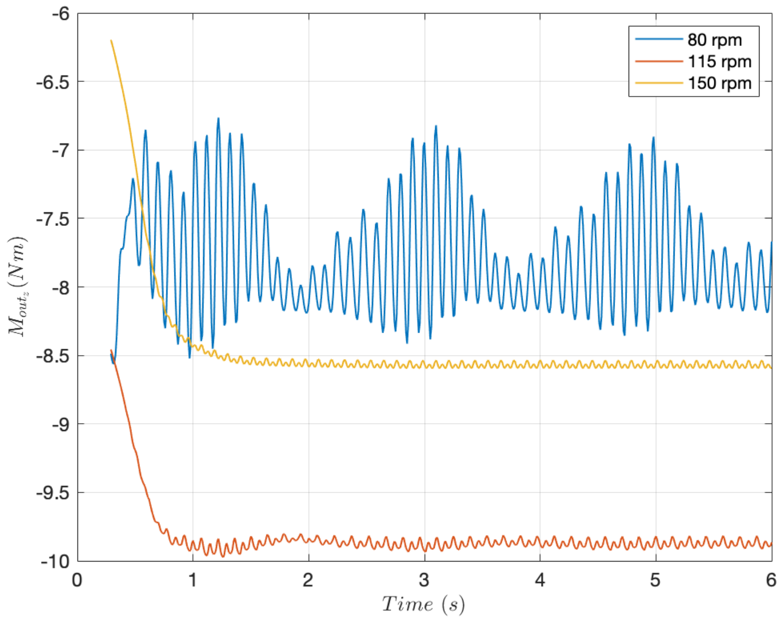

Figure 4.21: Comparison of extracted moment for three values of rotation speed

the other two cases. This means that the rotation speed of 115 rpm is the one nearest to the maximum value of autorotation moment. When studying the autorotation moment evolution with rotation speed with all these geometric parameters it is found that the rotation speed of 115 rpm is actually at the maximum. The same behavior regarding the oscillations is observed here as well.

Although the maximum rotation speed does not show the maximum moment extracted, the rotation speed also plays its role in the actual power extracted, which is actually the relevant parameter. The different power values obtained are:

$$P_{80} = 64\ W \qquad P_{115} = 118\ W \qquad P_{150} = 130\ W\ . \tag{4.7}$$

Therefore, when looking at the power output it seems that it is not actually the maximum extracted moment that will give the highest power output, and that the maximum power output will be at a higher rotation speed than the maximum autorotation moment. Nonetheless, it is noticeable the decay in the marginal increase in the power output once the maximum value of autorotation moment is reached.

To look for the maximum power, Figure 4.22 represents the evolution of the power output with the rotational speed, using a similar method as in Section 4.2. The maximum power is obtained at a rotational speed of 145 rpm. Therefore, the case of 150 rpm studied is actually in the decay after the maximum was obtained, but very close to it.

One last interesting result from this analysis concerns the lowest rotation speed case, that showed a big increase in oscillations both in the low frequency and high frequency scales. Figure 4.23 shows the aerodynamic forces of the rotor for this

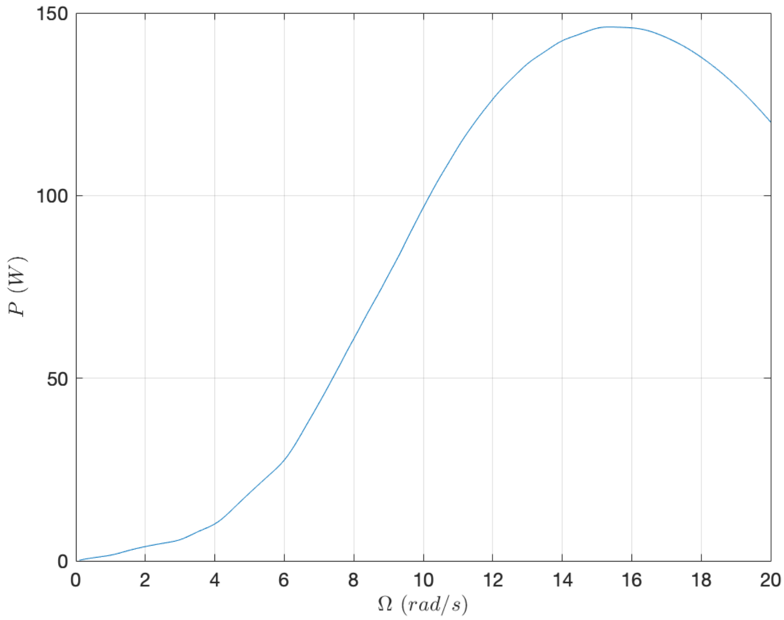

Figure 4.22: Power output evolution with the rotation speed

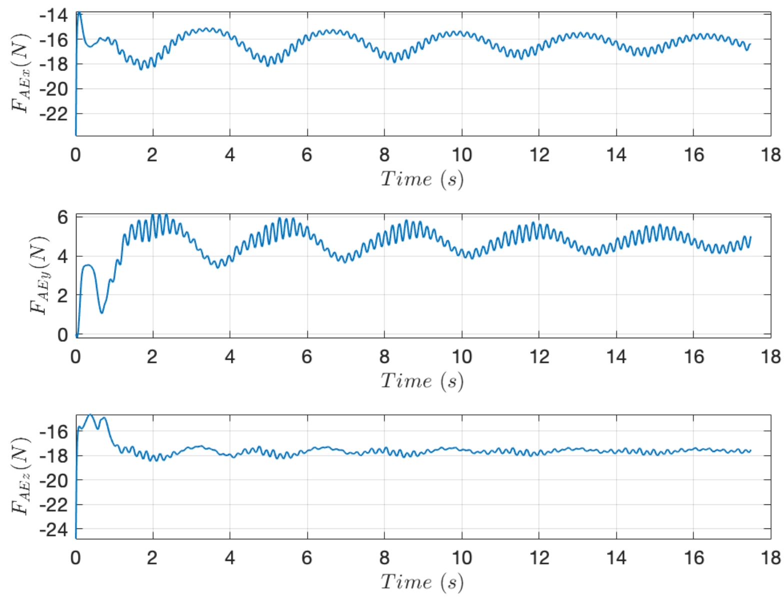

Figure 4.23: Aerodynamic forces of the rotor for a rotation speed of $\Omega = 80$ rpm. Earth frame

case in the Earth frame. It is obtained a higher lateral force component than in the base case, meaning that the magnitude of the lift asymmetry effect is higher at this lower rotation speed. Furthermore, the low frequency oscillation observed makes the machine not able to stay in equilibrium at a fixed point, but rather swinging around a point.

Table 4.3 sums up the results obtained for the three different cases of maximum rotation speed allowed.

	80 rpm	115 rpm	150 rpm
Extracted moment (Nm)	7.75	9.85	8.5
Power (W)	64	118	130
Lift in k_b (N)	25	33.75	36.25

Table 4.3: Results for the parametric study on the maximum rotation speed

4.6 Effect of the collective pitch angle

The last analysis done is to study the effect that the collective pitch angle has in the power output of the RAWES. The same values of the collective pitch angle used for Section 4.2 will be used now.

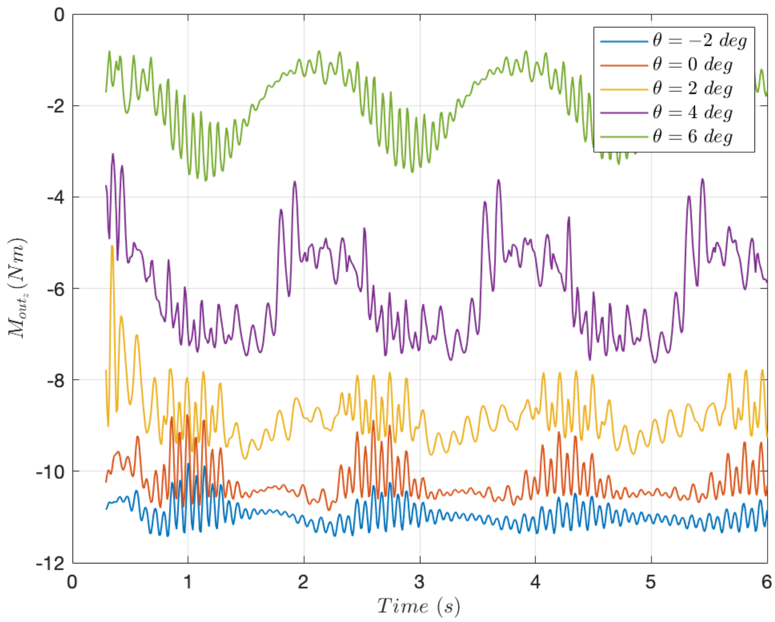

Figure 4.24: Extracted moment for several values of collective pitch angle

Figure 4.24 shows the moment extracted for the 5 different values of the collective pitch angle. This result may seem surprising. Since greater pitch angles would produce higher lift forces on each individual airfoil, it could be expected that the output of the system would also increase with the pitch angle. Contrary to this, the behavior of the system is that the lower the pitch angle the higher the extracted moment (in absolute value), but it is seen to be converging to a maximum value near pitch angle of around -2°. Lowering even more the pitch angle will end up reducing (in absolute value) again the moment.

This result goes totally in concordance to what was explained in Section 4.2, since the rotation speed of $\Omega = 115\ rpm$ is in the low rotation speed range in which lower angles of attack gave better results. It should be taken into account that this trend shown in Figure 4.24 is only valid for this very value of rotation speed and that at higher values of rotation speed the completely opposite trend would be expected, as according to the results of Figure 4.13.

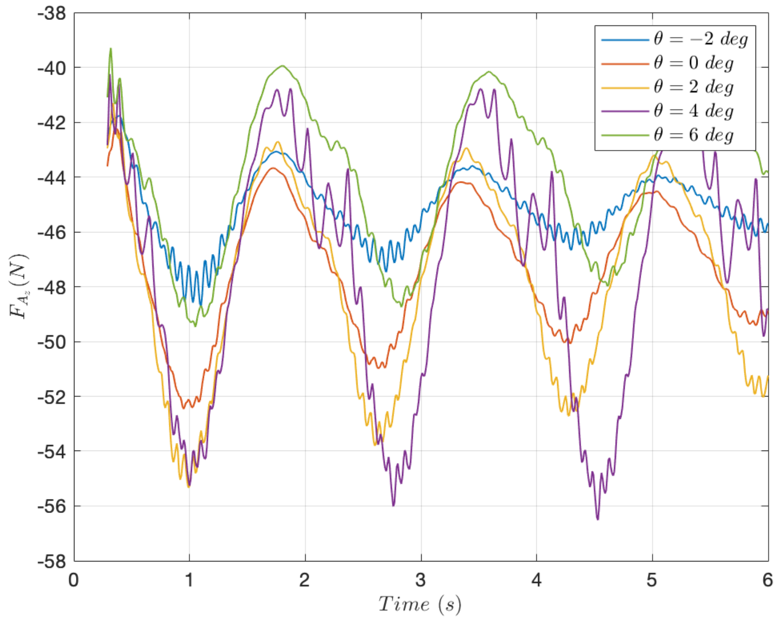

Figure 4.25: Rotor lift for several values of collective pitch angle. Body frame

Finally Figure 4.25 presents the result of the lift of the rotor, in the body frame, for all the values of the collective pitch angle studied. This result is very interesting, as the mean value of all cases seems to be very close to one another, while the low frequency oscillation in each case is quite different. Lower values of pitch angle show the least amplitude, and increasing the pitch angle seems to increase the oscillation in turn, although the peak is obtained for $\theta = 4^{\circ}$ and then decreases again for $\theta = 6^{\circ}$.

These results highlight the relevance of the pitch angle for obtaining the optimum design of the RAWES. For different values of collective pitch angle the equilibrium inclination of the rotor may change, so different times to converge to the equilibrium position could be expected. Nonetheless, in the case of using the collective pitch angle as active control this question would not be as relevant, although these results highlight the potential of the pitch angle to control the behavior of the rotorcraft, being a variable potentially easy to be changed with onboard actuators.

Chapter 5

Conclusions and further work

Contents

5.1 Conclusions

This project has been developed alongside a 6-months internship at *IFP Energies nouvelles*, at their Lyon's site. Therefore it has been a great opportunity to complete the educational background with an international experience, offering a great insight in how a company as big as *IFP Energies nouvelles* is organized and works. It has allowed as well for both a professional and personal development.

The nature of the thesis is an insight to what the research industry is doing. It is a kind of work different to any other industry, as it is much more difficult to set milestones and to track the progress, therefore planning has been very important. The knowledge from both the Bachelor and the Master have been necessary to complete this work and have been successfully put into practice. The conclusions of the work carried out are presented hereunder.

5.1.1 Conclusions of the dynamic simulator

- A dynamic simulator for RAWES has been developed and successfully built into the existing modules of LAKSA in Matlab. This enhances the usefulness of LAKSA, which now is equipped with modules to cover all current designs in the actual state of the art for Airborne Wind Energy Systems.
- The dynamic simulator has been built with a high degree of generalization, making it possible to have parametrized in a single *Matlab* file all the variables relevant to the machine.

- The importance of several parameters has been stated. Namely the need to include the inflow model in the aerodynamic model, the number of blades, or the collective pitch angle.
- RAWES are very dynamic systems, and autorotation may have different equilibrium points, some stable and some unstable.
- While at high rotational speeds positive pitch angles provide the best results, at low rotational speeds it will be low and even negative pitch angles the ones providing the best results. To be able to exploit the maximum of this technology, a very careful structural design is required in order to allow for higher rotational speeds that do not tear down the rotor.
- At high rotational speeds the power generated can be much higher than at low rotational speeds. Therefore, a stiffer structure that would allow the machine to bear such big efforts would have be a great advantage.
- The inflow model has a big relevance in the results shown. It is required in order to not overestimate the results (overestimation of around 18% in this work).
- With the design and flight parameters used, corresponding to the prototype in [4], and not optimizing them for each case, the 4 and 5 blades design show the best results. To be able to select the best between a 3, 4 or 5 blades design in order to build prototypes, all design and flight parameters should be optimized for each case, and then compare the optimized results between one another.

5.2 Further work

This dynamic simulator for Rotorcraft Airborne Wind Energy Systems has been built to provide a better understanding of all the physics involved in the behavior of a rotorcraft in autorotation. In this respect, and being one of the first models to address this problem for its use in the energy industry, it's been built fairly simple in order to be a tool from the beginning.

But this simulator should be completed, so as further work two main characteristics are left to be implemented, whose necessity for the improvement of the simulator has been highlighted all over this thesis:

- **Flapping model**. The flapping movement of the blades is a natural movement arising from the aerodynamic characteristics of the rotor, where the blades try to cone up to balance the aerodynamic and centrifugal forces. Not allowing this movement causes, as first seen by de la Cierva in his firsts autogyros, a net force sideward. This would not allow the rotor to stay fixed at a point without active control or an external element such as the anchor kite used in this model. Since commercial applications for RAWES are very likely to include flap hinges, its implementation in the simulator would help enhance its usability until further stages of the development. Furthermore, if flap hinges are not used, even the flexibility of the materials allow the flapping movement, up to a different extent depending on the flexibility. In this model everything is rigid, so flexibility is not accounted for, hence highlighting the relevance of including the flapping movement in the model.

- **Control capabilities**. Obtaining energy from the wind with a system like the one developed here at a global scale will only be possible if all parameters are optimized. Apart from the optimization of the design, an active control would be needed to adapt, for example, the pitch of the blades to make the rotor stay in its optimum performance point. These control capabilities have been deeply studied for other types of AWES, as they are implemented for example in the rest of modules of LAKSA. Furthermore, control opens the research even more to study the optimization of variables and trajectories for the best exploitation of the technology.

All in all, the simulator is able to show the potential of this technology and will help the user to study in depth the effect of any change in the design.

Bibliography

[1] Hannah Ritchie and Max Roser. Renewable energy. *Our World in Data*, 2020. `https://ourworldindata.org/renewable-energy`.

[2] Wind Europe. Wind energy in europe in 2019, trends and statistics. 2020. `https://windeurope.org`.

[3] Antonello Cherubini, Andrea Papini, Rocco Vertechy, and Marco Fontana. Airborne wind energy systems: A review of the technologies. *Renewable and Sustainable Energy Reviews*, 51:1461 – 1476, 2015.

[4] Christof Beaupoil. Practical experiences with a torsion based rigid blade rotary airborne wind energy system with ground based power generation. 2019.

[5] KiteGen. Kitegen research. `www.kitegen.com`.

[6] Makani Power. Makani power: Our journey. `www.makanipower.com/journey`.

[7] J Gordon Leishman. Development of the autogiro: A technical perspective. *Journal of Aircraft*, 41(4):765–781, 2004.

[8] A Cuerva, JL Espino, O López, J Meseguer, and A Sanz. Teoría de los helicópteros. *Serie de Ingeniería y Técnica Aeroespacial, Universidad Politécnica de Madrid, Madrid, España*, 2009.

[9] Y Murakami and SS Houston. Dynamic inflow modelling for autorotating rotors. *The Aeronautical Journal*, 112(1127):47–53, 2008.

[10] SS Houston and RE Brown. Rotor-wake modeling for simulation of helicopter flight mechanics in autorotation. *Journal of aircraft*, 40(5):938–945, 2003.

[11] Jim Skea. Roadmap 2050: A practical guide to a prosperous, low-carbon europe, european climate foundation (2010). *Environmental Innovation and Societal Transitions*, 3, 06 2012.

[12] R. Pichs-Madruga Y. Sokona E. Farahani S. Kadner K. Seyboth A. Adler I. Baum S. Brunner P. Eickemeier B. Kriemann J. Savolainen S. Schlömer C. von Stechow T. Zwickel Edenhofer, O. and J.C. Minx (eds.). Summary for policymakers, in: Climate change 2014: Mitigation of climate change, contribution of working group iii to the fifth assessment report of the intergovernmental panel on climate change. *IPCC*, 2014.

[13] Jordan Wilkerson. Reconsidering the risks of nuclear power. *Harvard Blog Special Edition: Dear Madam/Mister President*, 2016.

[14] Lazard's levelized cost of energy analysis. *Lazard*, 2018.

[15] IEA ETSAP. Hydropower - energy technology systems analysis programme. *IEA ETSAP - Technology Brief*, 2010.

[16] IREA IRENA. Renewable power generation costs in 2018. *Report, International Renewable Energy Agency, Abu Dhabi*, 2019.

[17] K. Caldeira. Seasonal, global wind resource diagrams. `www.skywindpower.com`.

[18] R. ODoherty and B. Roberts. Application of us upper wind data in one design of tethered wind energy systems. 01 1982.

[19] Bryan Roberts and Zaiping Pan. New means of generating electricity using upper atmospheric wind. 20:31–37, 01 1999.

[20] Bryan Roberts, David Shepard, Ken Caldeira, Elizabeth Cannon, David Eccles, Albert Grenier, and Jonathan Freidin. Harnessing high-altitude wind power. *Energy Conversion, IEEE Transactions on*, 22:136 – 144, 04 2007.

[21] Miles L. Loyd. Crosswind kite power (for large-scale wind power production). *Journal of Energy*, 4(3):106–111, 1980.

[22] Ivan Argatov, P. Rautakorpi, and R. Silvennoinen. Estimation of the mechanical energy output of the kite wind generator. *Renewable Energy*, 34:1525–1532, 06 2009.

[23] Paul Williams, Bas Lansdorp, and Wubbo Ockels. Optimal cross-wind towing and power generation with tethered kites. *Journal of Guidance Control and Dynamics - J GUID CONTROL DYNAM*, 31:81–93, 01 2008.

[24] KitePower. Kitepower 2.0 website. `www.kitepower.eu`.

[25] G Sanchez. Dynamics and control of single-line kites. *The Aeronautical Journal*, 110(1111):615–621, 2006.

[26] R Borobia, G Sanchez-Arriaga, A Serino, and R Schmehl. Flight-path reconstruction and flight test of four-line power kites. *Journal of Guidance, Control, and Dynamics*, 41(12):2604–2614, 2018.

[27] Gonzalo Sánchez-Arriaga, Manuel García-Villalba, and Roland Schmehl. Modeling and dynamics of a two-line kite. *Applied Mathematical Modelling*, 47:473–486, 2017.

[28] A Pastor-Rodríguez, Gonzalo Sánchez-Arriaga, and M Sanjurjo-Rivo. Modeling and stability analysis of tethered kites at high altitudes. *Journal of Guidance, Control, and Dynamics*, 40(8):1892–1901, 2017.

[29] J Alonso-Pardo and Gonzalo Sánchez-Arriaga. Kite model with bridle control for wind-power generation. *Journal of Aircraft*, 52(3):917–923, 2015.

[30] G. Sánchez-Arriaga, A. Pastor-Rodríguez, M. Sanjurjo-Rivo, and R. Schmehl. A lagrangian flight simulator for airborne wind energy systems. *Applied Mathematical Modelling*, 69:665 – 684, 2019.

[31] Sadaf Mackertich. Dynamic modeling of autorotation for simultaneous lift and wind energy extraction. 2016.

[32] Jochem De Schutter, Rachel Leuthold, and Moritz Diehl. Optimal control of a rigid-wing rotary kite system for airborne wind energy. In *2018 European Control Conference (ECC)*, pages 1734–1739. IEEE, 2018.

[33] Wayne Johnson. *Rotorcraft Aeromechanics*. Cambridge Aerospace Series. Cambridge University Press, 2013.

[34] Hermann Glauert. The theory of the autogyro. *The Aeronautical Journal*, 31(198):483–508, 1927.

[35] CNH Lock. *Further development of autogyro theory*. HM Stationery Office, 1927.

[36] J. B. Wheatley. An aerodynamic analysis of the autogiro rotor with a comparison between calculated and experimental results. *National Advisory Committee for Aeronautics*, Report No. 487, 1934.

[37] SS Houston. Validation of a rotorcraft mathematical model for autogyro simulation. *Journal of Aircraft*, 37(3):403–409, 2000.

[38] SS Houston. Analysis of rotorcraft flight dynamics in autorotation. *Journal of guidance, control, and dynamics*, 25(1):33–39, 2002.

[39] ROBERT TN Chen. A survey of nonuniform inflow models for rotorcraft flight dynamics. 1989.

[40] R E Sheldahl and P C Klimas. Aerodynamic characteristics of seven symmetrical airfoil sections through 180-degree angle of attack for use in aerodynamic analysis of vertical axis wind turbines. 3 1981.

[41] Dale Pitt and David Peters. Theoretical prediction of dynamic-in ow derivatives. *Vertica*, 5, 01 1981.

[42] RE Brown and SS Houston. Comparison of induced velocity models for helicopter flight mechanics. *Journal of aircraft*, 37(4):623–629, 2000.

[43] Giovanni Vergnano. Rotokite: A different approach for the exploitation of the high-altitude wind. 2013.

[44] D Rezgui and MH Lowenberg. On the nonlinear dynamics of a rotor in autorotation: a combined experimental and numerical approach. *Philosophical Transactions of the Royal Society A: Mathematical, Physical and Engineering Sciences*, 373(2051):20140411, 2015.